**VILNIUS UNIVERSITY**
**FACULTY OF CHEMISTRY AND GEOSCIENCES**
**INSTITUTE OF CHEMISTRY**
**DEPARTMENT OF INORGANIC CHEMISTRY**

**Gabija Janušauskaitė**
Chemistry
Master thesis

# SYNTHESIS AND INVESTIGATION OF THE LUMINESCENT PROPERTIES OF $NaAlGeO_4$ DOPED WITH $Bi^{3+}$, $Dy^{3+}$, $Eu^{3+}$, $Pr^{3+}$, $Sm^{3+}$, AND $Tb^{3+}$ IONS

Scientific adviser
doc. dr. Martynas Misevičius

Vilnius 2025

VILNIAUS UNIVERSITETAS
CHEMIJOS IR GEOMOKSLŲ FAKULTETAS
CHEMIJOS INSTITUTAS
NEORGANINĖS CHEMIJOS KATEDRA

**Gabija Janušauskaitė**
Chemija
Magistro baigiamasis darbas

# $Bi^{3+}$, $Dy^{3+}$, $Eu^{3+}$, $Pr^{3+}$, $Sm^{3+}$, IR $Tb^{3+}$ JONAIS LEGIRUOTO $NaAlGeO_4$ SINTEZĖ IR LIUMINESCENCINIŲ SAVYBIŲ TYRIMAS

Darbo vadovas
doc. dr. Martynas Misevičius

Vilnius 2025

# CONTENTS

# LIST OF ABBREVIATIONS

CIE – International Commission on Illumination.
CT – Charge Transfer.
IR – Infrared Radiation.
LED – Light Emitting Diodes.
NIR – Near-Infrared Radiation.
OLED – Organic Light Emitting Diodes.
PerL – Persistent Luminescence.
PL – Photoluminescence.
QY – Quantum Yield.
UV – Ultraviolet Radiation.
UVA – Ultraviolet A-Rays.
XRD – X-Ray Diffraction.

# INTRODUCTION

Photoluminescent (PL) phosphors typically consist of a host material and an emitter, with the PL colour primarily determined by the emitter. However, choosing an appropriate host material is also crucial for achieving high-efficiency phosphors activated by rare-earth ions. Germanate compounds have attracted significant attention as hosts for phosphors due to their low synthesis temperatures and excellent physical and chemical properties. These materials often exhibit high thermal stability and exceptional luminescence properties, making them attractive for applications in light-emitting diodes (LEDs), displays, biomedical imaging, solar cells and more [1–6]. Recent studies have introduced $LiYGeO_4:Bi^{3+}$ as a novel persistent luminescent material with a long-lasting ultraviolet A (UVA) afterglow, persisting over 300 hours after 10 minutes of 254 nm irradiation [7]. Tiansong Dai et al. also found that $LiYGeO_4:Eu^{3+}$ displays strong persistent luminescence (PerL) peaks at 354 nm and 611 nm, with red afterglow lasting over 21 hours at low doping concentrations [8]. Other related compounds include $LiYGeO_4$ doped with $Bi^{3+}$ [9,10], $Eu^{3+}$ [8,9,11,12], $Dy^{3+}$ [13], $Tb^{3+}$ [12,14–17], $Pr^{3+}$ [18] and co-doped with $Bi^{3+}/Pr^{3+}$ [19]. $NaYGeO_4$ doped with $Eu^{3+}$ [20–24], $Dy^{3+}$ [22], $Sm^{3+}$ [22], $Tb^{3+}$ [20,23] and $Bi^{3+}$ [20]. Also, various other germanates like $LiAlGeO_4:Eu^{3+}$, $Bi^{3+}$ [25], $Cr^{3+}$ [26], and $LiScGeO_4:Bi^{3+}$ [27,28], $Cr^{3+}$ [29–31], all of which demonstrate the suitability of germanates as hosts for luminescent materials. This potential has led to interest in $NaAlGeO_4$ as a matrix for developing new luminescent materials. $NaAlGeO_4$ crystallizes in the monoclinic system with the $P2_1/n$ space group (no. 14) and has cell parameters of $a = 8.78300$ Å, $b = 15.43200$ Å, $c = 8.25200$ Å and $\gamma = 90.090°$ [32,33]. Despite its well-characterized crystal structure, there is surprisingly little information available on the luminescent properties of $NaAlGeO_4$ in the scientific literature.

Lanthanoids such as dysprosium (Dy), europium (Eu), praseodymium (Pr), terbium (Tb) and samarium (Sm) are widely used in the synthesis of PL phosphors due to their excellent luminescent properties. These rare-earth elements are known for their ability to provide long-lasting afterglow [8,15,28,34,35]. Dysprosium and europium, for instance, are commonly used for their bright and long-duration emission in the visible spectrum [8,36], with europium often providing red emission ($^5D_0 \rightarrow {}^7F_2$ transition at 611 nm) and dysprosium offering yellow ($^4F_{9/2} \rightarrow {}^6H_{13/2}$ at 574 nm), blue ($^4F_{9/2} \rightarrow {}^6H_{15/2}$ at 480 nm) and red ($^4F_{9/2} \rightarrow {}^6H_{11/2}$ at 666 nm) emissions. Praseodymium ions are intriguing optical dopants because of their various multicolour 4f-4f luminescent transitions [37]. Specifically, the $^3P_0 \rightarrow {}^3H_6$ transition at 645 nm provides efficient orange-red emissions. Samarium is known for its high lumen output, excellent colour purity and strong radiation stability [38]. $Sm^{3+}$ doped germanates emit efficient orange-red light at 600 nm ($^4G_{5/2} \rightarrow {}^6H_{9/2}$ transition). Terbium is used as a long afterglow phosphor emitting green light ($^5D_4 \rightarrow {}^7F_5$ at 549 nm) [15]. However, the high cost and limited availability of lanthanoids present significant challenges for large-scale and cost-effective production of PL materials. To address this, the synthesis of $NaAlGeO_4$ with bismuth as a dopant was also explored. The enduring UVA afterglow, combined with the photostimulated persistent luminescence capability, establishes $Bi^{3+}$ doped germanates as a significant component of persistent luminescence materials in the UVA spectral region [10,28]. Bismuth (blue emission $^3P_1 \rightarrow {}^1S_0$ at 420 nm), being more abundant and less expensive, offers a promising alternative for developing efficient and affordable luminescent materials, potentially reducing reliance on costly lanthanoids without compromising performance.

Motivated by the research mentioned above, $NaAlGeO_4$ was selected as the host matrix, with $Bi^{3+}$, $Dy^{3+}$, $Eu^{3+}$, $Pr^{3+}$, $Sm^{3+}$, and $Tb^{3+}$ ions as the activators. The aim of this work is to synthesise a series of $Na_{1-x}AlGe_{1-0.5x}O_4$-based phosphors doped with varying concentrations of trivalent $Bi^{3+}$,

$Dy^{3+}$, $Eu^{3+}$, $Pr^{3+}$, $Sm^{3+}$, and $Tb^{3+}$ ions using the high-temperature solid-state method, and to investigate their luminescence properties.

Objectives:

1. To synthesise $NaAlGeO_4$ phosphors doped with varying concentrations of $Bi^{3+}$, $Dy^{3+}$, $Eu^{3+}$, $Pr^{3+}$, $Sm^{3+}$, and $Tb^{3+}$ ions using the high-temperature solid-state synthesis method and characterise the samples through X-ray diffraction.
2. To examine the excitation and emission spectra of the doped $NaAlGeO_4$ phosphors.
3. To investigate the luminescence decay times of the synthesised samples.
4. To evaluate the quantum efficiencies of the synthesised samples.

# 1. LITERATURE REVIEW

## 1.1 Luminescence

Luminescence emission occurs when a material absorbs energy from an external source, such as ultraviolet (UV) or infrared (IR) radiation, an electron beam, a chemical reaction, or other means. This energy excites an electron from its ground state (the lowest energy level) to a higher-energy excited state. As the excited state is inherently unstable, the electron eventually returns to the ground state, releasing the absorbed energy in the form of light, heat, or a combination of both. This excitation process involves only the outer electrons orbiting the atomic nuclei. The efficiency of luminescence depends on how effectively the absorbed energy is converted into light. Only a limited number of materials exhibit sufficiently high luminescence efficiency to be considered useful for practical applications. Luminescence can occur in materials across all states of matter, including gases, liquids, crystalline and amorphous solids, polymers, glasses, as well as organic and inorganic substances [39].

Depending on the source of excitation energy and the characteristics of the emitted light, luminescence can be categorised into several types, some of them are outlined in **Table 1** [40].

**Table 1.** Classification of luminescence based on the source of excitation.

| Type of Luminescence | Source of Excitation | Example / Application |
|---|---|---|
| Thermoluminescence | Heating of a previously irradiated material | Radiation dosimetry, archaeological/geological dating, gem authentication |
| Radioluminescence | Ionising radiation (e.g. X-rays, gamma rays, alpha/beta particles) | Self-luminous watches, emergency signage, instrument dials |
| Cathodoluminescence | Electron beam excitation | Cathode ray tube displays, scanning electron microscopy |
| Triboluminescence (Mechanoluminescence) | Mechanical action (e.g. stretching, tearing, crushing) | Seen in sugar crystals, adhesive tape, and some crystals |
| Chemiluminescence | Chemical reactions | Glow sticks, luminol in forensics, bioassays |
| Sonoluminescence | Ultrasonic wave excitation | Studied in fluid mechanics and cavitation physics |
| Electroluminescence | Electric field | LEDs, OLEDs, electroluminescent panels in watches and displays |
| Photoluminescence | Light (usually UV or visible) | Fluorescent dyes, plasma displays, whitening agents, solar energy materials |
| Persistent Luminescence | Very slow decay of emission after excitation | Glow-in-the-dark materials, emergency exit signs, safety markings |
| Bioluminescence | In vivo biochemical reaction | Gene assays, detection of protein-protein interactions |

Luminescence is generally categorised based on the duration of the emitted radiation into fluorescence and phosphorescence. Fluorescence is a fast-emitting process that ceases almost immediately once excitation stops, typically with a lifetime of less than $10^{-6}$ seconds. It is a radiative transition between two spin-allowed multiplets, occurring from the lowest vibrational level of the first excited singlet state to the singlet ground state. In molecules, fluorescence is commonly observed in conjugated systems containing delocalised $\pi$-electrons, which efficiently absorb and subsequently emit light. The emission spectrum of such molecules can be influenced by various factors, including the solvent environment, pH, and the presence of other molecules. Fluorescent substances are widely used as markers or probes for tracking molecules in biological systems and are also key in analytical techniques such as fluorescence microscopy and flow cytometry [39].

Phosphorescence, on the other hand, is a longer-lasting luminescence that persists for more than $10^{-6}$ seconds after the excitation source has been removed. It occurs between spin-forbidden multiplets – specifically from an excited triplet state to the singlet ground state. Because this transition is quantum-mechanically forbidden by spin selection rules, phosphorescence typically lasts much longer than fluorescence. In some cases, phosphorescence can continue for several hours or even days. Another mechanism responsible for phosphorescence involves the trapping of electrons and/or holes in energy traps. These localised charge carriers are gradually released through thermal activation, and upon recombination, the stored energy is emitted as light. This form of phosphorescence, often referred to as persistent luminescence, is characterised by its ability to emit light for extended periods after the excitation source has been removed. Phosphorescent materials are utilised in applications such as light-emitting diodes (LEDs), bioimaging, temperature sensors, and emergency lighting systems [40].

As illustrated in **Figure 1**, the energy level structure of rare-earth ions embedded in a crystal lattice is primarily governed by Coulomb interactions and spin-orbit coupling, both of which are relatively strong and comparable in magnitude – typically amounting to several tens of thousands of wavenumbers [41]. In comparison, the Stark splitting introduced by the crystal field is considerably weaker, usually in the range of several hundred wavenumbers. Due to the shielding effect of the outer 5s and 5p electrons, the inner 4f electrons of rare-earth ions are only weakly influenced by the surrounding crystal environment. As a result, their electronic energy levels remain relatively unaffected by changes in host lattice and retain a strong resemblance to those of the corresponding free-ion (triply ionised) states in the gas phase. This preservation of free-ion character makes it possible to apply atomic-like models to solid-state systems, with minor adjustments for the influence of the crystal field.

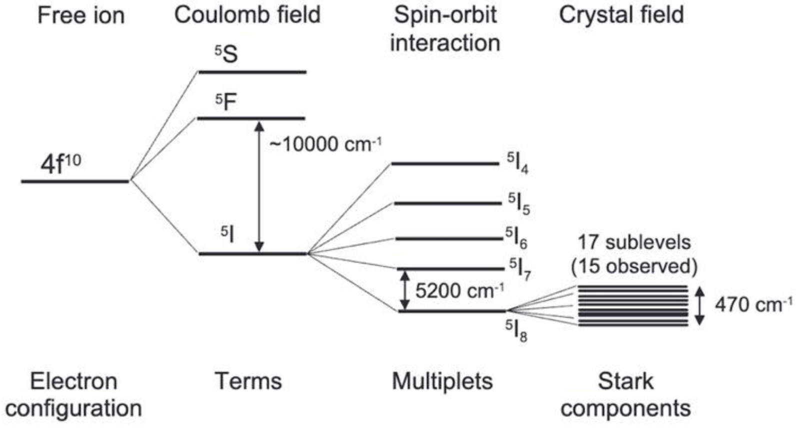

**Figure 1.** The crystal field effect on the splitting of energy levels within the 4f electron shell of lanthanide ions [41].

Given this, the well-established Dieke diagram proves to be a valuable and reliable tool for predicting and analysing the spectroscopic behaviour of rare-earth ions in various host materials. It allows for a visual representation of the relative energy positions of multiplet states for different lanthanide ions and gives a useful approximation of the Stark sub-level distributions that occur in crystalline environments. Although Stark splitting does vary depending on the specific site symmetry and field strength in the host, the general layout of the Dieke diagram remains valid and informative across different matrices. **Figure 2** presents a simplified version of this diagram, highlighting only the energy levels pertinent to the rare-earth ions discussed in this work, particularly those with potential for tunable visible emission [41].

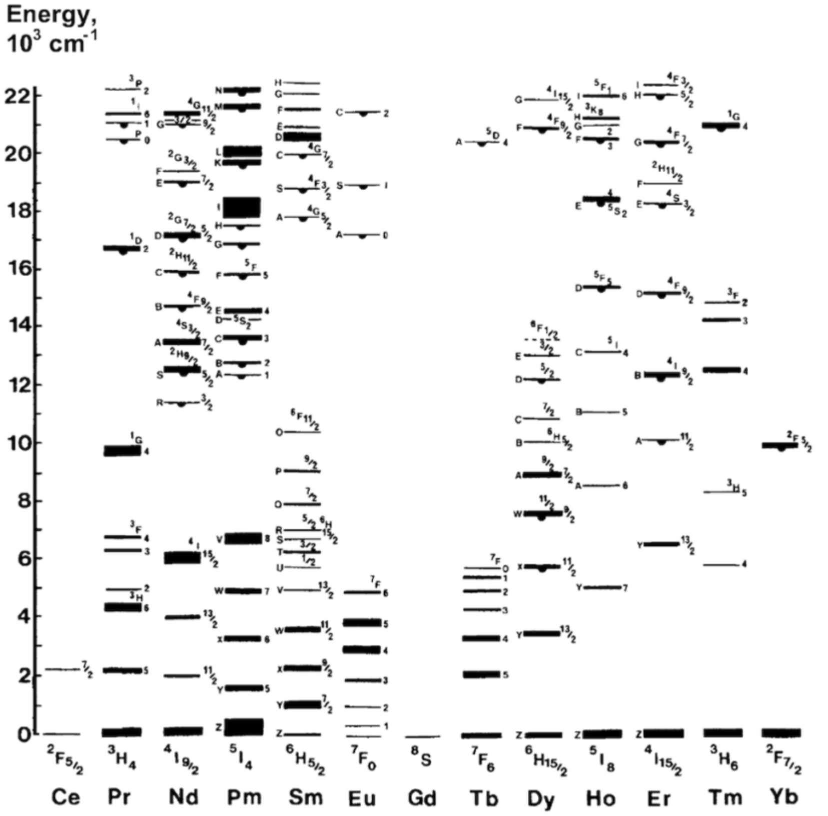

**Figure 2.** Simplified Dieke diagram (rare-earth ions in $LaCl_3$) [41].

### 1.1.1 Luminescent properties of $Bi^{3+}$

The energy levels of $Bi^{3+}$ (bismuth(III)) ions are governed by the electron configuration of the ion, which in the trivalent state is $[Xe]4f^{14}5d^{10}6s^2$. This closed-shell configuration results in a singlet ground state ($^1S_0$), with excited states derived primarily from the promotion of one of the 6s electrons to the 6p orbital. The most commonly observed transitions occur between the $^1S_0$ ground state and the excited $^1P_1$ and $^3P_1$ states, with the $^1S_0 \rightarrow {}^1P_1$ transition being parity-allowed and typically responsible for luminescence in certain host lattices (**Figure 3**) [42]. However, in most cases, the luminescence from $Bi^{3+}$ is relatively weak due to low oscillator strengths and the influence of non-radiative decay processes. Despite this, $Bi^{3+}$-doped materials can exhibit broadband emission in the UV to visible range, often from blue to yellow, depending on the local coordination environment, crystal field strength, and degree of covalent interaction between $Bi^{3+}$ and surrounding anions such as oxygen [7,10].

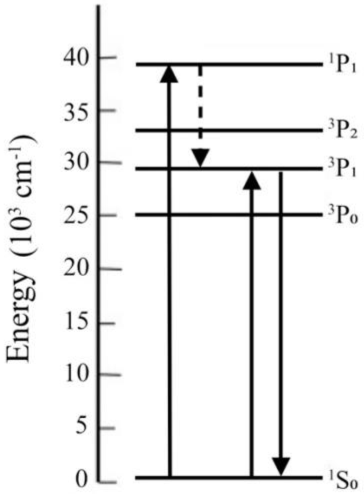

**Figure 3.** Energy level diagram of $Bi^{3+}$ in Bi-doped SrO–$B_2O_3$ [42].

The emission and excitation behaviour of $Bi^{3+}$ are highly sensitive to its site symmetry and coordination number within the host lattice. For example, when $Bi^{3+}$ is coordinated in a distorted or asymmetric environment, it may lead to splitting of energy levels, thereby broadening the emission band. This makes $Bi^{3+}$ a useful sensitiser or co-dopant in phosphor systems, where it can facilitate energy transfer to other activators such as $Eu^{3+}$ [9], $Tb^{3+}$ [16], or $Pr^{3+}$ [19] enhancing overall emission intensity and colour tunability. Additionally, the relatively large ionic radius of $Bi^{3+}$ (103 pm) allows it to substitute for other large monovalent or trivalent cations, such as $Na^+$ or $K^+$, in a wide range of oxide and germanate hosts. This substitution can induce structural distortion, affecting the crystal field and further tuning the emission profile. As a result, $Bi^{3+}$ is being explored not only for its intrinsic luminescence but also for its ability to modify local symmetry, act as a crystal field modifier, and participate in energy transfer mechanisms in advanced optical materials, including white light phosphors [9], scintillators [43], and anti-counterfeiting [44].

### 1.1.2 Luminescent properties of lanthanoids

The energy level diagram of the $Dy^{3+}$ (dysprosium) ion at **Figure 4** illustrates its characteristic excitation and emission behaviour, typical of trivalent lanthanide ions. Upon excitation at 375 nm, electrons are promoted from the ground state $^6H_{15/2}$ to higher-lying excited states, most notably the $^4F_{9/2}$ level. From this excited state, the system undergoes non-radiative relaxation – primarily through phonon interactions with the surrounding host lattice – redistributing energy to lower-energy states without photon emission. Radiative transitions then occur, giving rise to several sharp, well-defined emission lines, which originate from intra-4f electronic transitions. These transitions are formally forbidden by the Laporte rule, which states that electronic transitions are only allowed if they involve a change in parity (i.e., from a symmetric to an antisymmetric orbital, or vice versa). However, in $Dy^{3+}$ ions, the intensity of these formally forbidden transitions is enhanced through mixing with higher-lying electronic states of different spatial symmetry and through asymmetries in the crystal field environment [45].

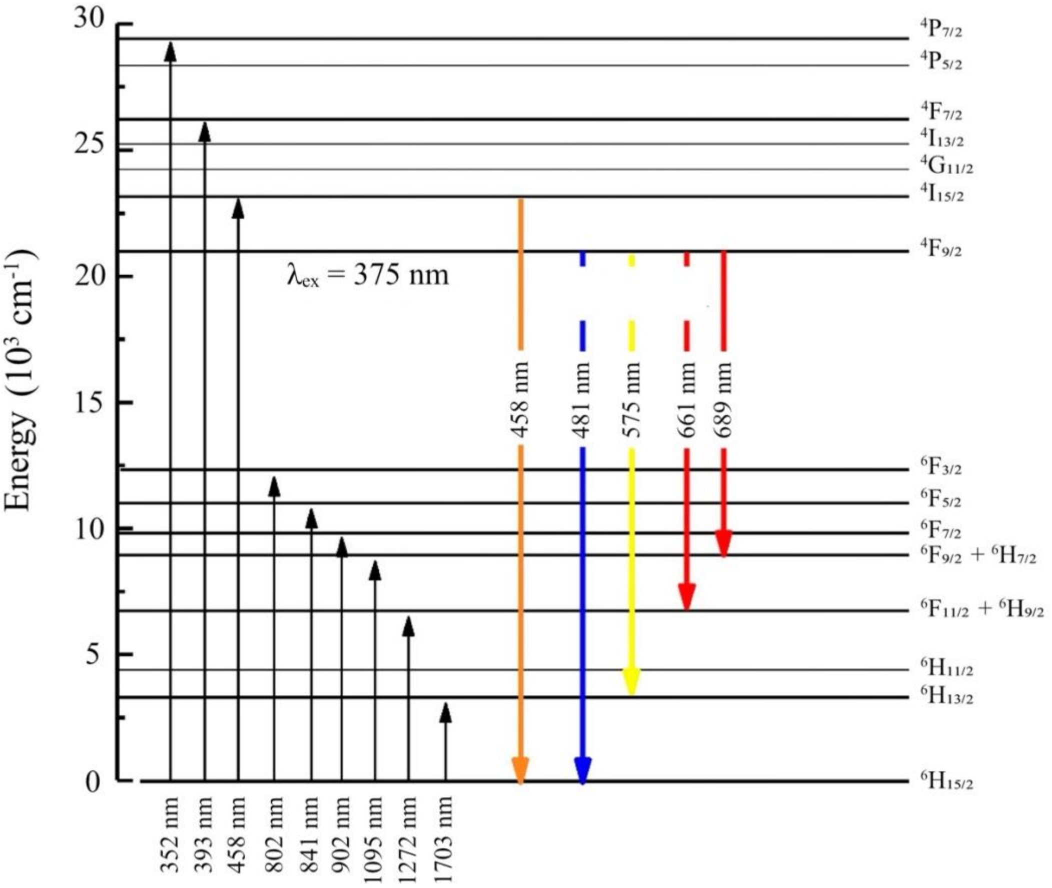

**Figure 4.** Energy level diagram of $Dy^{3+}$ in Dy-doped lithium–aluminium–borate glass [45].

In $Dy^{3+}$ ions, the 4f orbitals are effectively shielded by the outer 5s and 5p electron shells, which limits their interaction with the surrounding crystal field. This weak coupling with the host lattice results in minimal splitting of the 4f energy levels and gives rise to sharp, well-defined emission lines. The most prominent luminescent transitions from the $^4F_{9/2}$ state are to various levels of the $^6H_J$ ground multiplet. These include the $^4F_{9/2} \rightarrow {}^6H_{15/2}$ transition at 481 nm (blue), $^4F_{9/2} \rightarrow {}^6H_{13/2}$ at 575 nm (yellow), and weaker red emissions such as $^4F_{9/2} \rightarrow {}^6H_{9/2}$ and $^6H_{7/2}$ at 661 nm and 689 nm, respectively [45]. The simultaneous presence of blue and yellow emissions is particularly valuable, as their combination can produce white light. This makes $Dy^{3+}$ a highly promising activator ion for use in white-light-emitting phosphors and solid-state lighting applications [46].

The $Eu^{3+}$ (europium) ion exhibits a well-defined luminescence profile arising from intra-4f electronic transitions, which are characteristic of trivalent lanthanides (**Figure 5**). Upon excitation, typically into higher-lying 4f states such as $^5L_6$ or $^5D_2$, or via charge-transfer bands, rapid non-radiative relaxation channels the excitation energy to the long-lived $^5D_0$ state. Radiative transitions from this level to the $^7F_J$ (J = 0-6) ground multiplet produce a series of sharp emission lines that are largely unaffected by the host lattice, owing to the effective shielding of the 4f electrons by the outer 5s and 5p orbitals [47]. However, the intensity and splitting of these lines can be highly dependent on the local environment, particularly the symmetry of the crystallographic site occupied by the emitting ion, which influences the strength of the crystal field interactions. The most intense emission, typically observed around 612 nm, corresponds to the electric dipole $^5D_0 \rightarrow {}^7F_2$ transition, which is highly sensitive to the local symmetry and is enhanced in non-centrosymmetric environments. In contrast, the magnetic dipole $^5D_0 \rightarrow {}^7F_1$ transition, at 587 nm, is relatively insensitive to symmetry and is often used as a reference. The intensity ratio between these transitions provides valuable insight into the coordination environment of Eu$^{3+}$. Due to its intense red emission, narrow spectral linewidths, and high colour purity, Eu$^{3+}$ is widely utilised as a red-emitting activator in phosphor materials for solid-state lighting, display technologies [23,24], and bioimaging applications [48].

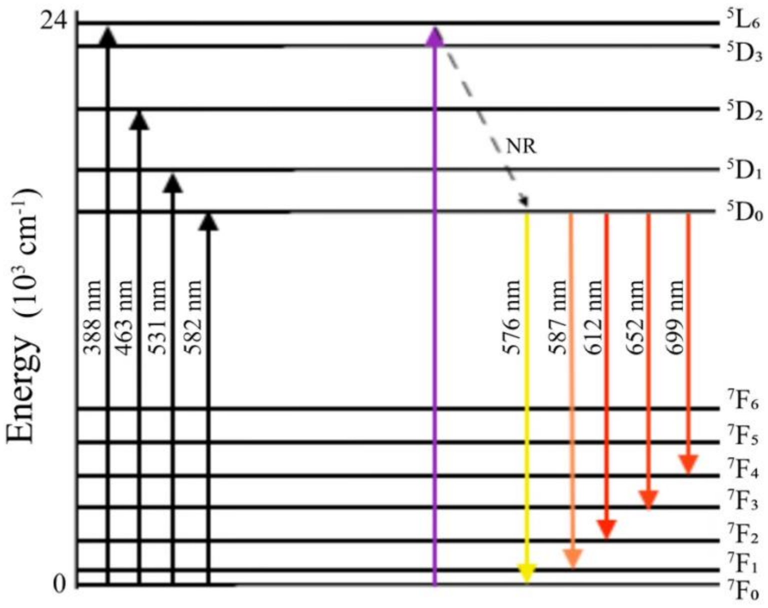

**Figure 5.** Energy level diagram of Eu$^{3+}$ at $\lambda_{ex}$ = 390 in Eu-doped $Li_2O$–$Na_2O$–$B_2O_3$ glass [47]. NR refers to non-radiative transitions.

The Pr$^{3+}$ (praseodymium) ion displays a complex luminescence behaviour due to its rich energy level structure (**Figure 6**). Unlike many other trivalent lanthanides, Pr$^{3+}$ can exhibit efficient emission from multiple excited states, depending on the host matrix and excitation conditions. Upon excitation, electrons are promoted from the ground state ($^3H_4$) to higher energy levels, followed by rapid non-radiative relaxation to the $^3P_0$ and, to a lesser extent, the $^3P_1$ level. Notable visible emissions include $^3P_0 \rightarrow {}^3H_5$ (~537 nm, green) and $^3P_0 \rightarrow {}^3H_6$ (~603 nm, orange). Additional orange and red emissions arise from $^3P_0 \rightarrow {}^3F_2$ (~636 nm) and $^3P_0 \rightarrow {}^3F_4$ (~700 nm), while weak emissions from $^3P_1$ may also be observed in the red region depending on the host [49]. These intra-4f transitions are only weakly influenced by the crystal field due to shielding by outer 5s and 5p orbitals, resulting in narrow, well-defined emission bands. The combination of green and red emissions makes Pr$^{3+}$ a suitable candidate for visible-light-emitting phosphors and solid-state laser materials [18,50].

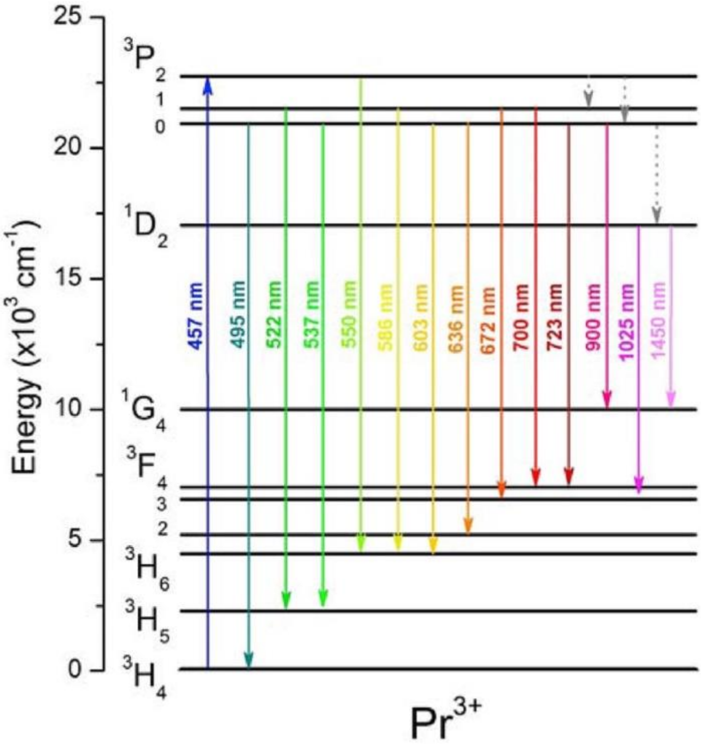

**Figure 6.** Pr$^{3+}$ energy level diagram in Pr-doped Pb(In$_{1/2}$Nb$_{1/2}$)O$_3$–Pb(Mg$_{1/3}$Nb$_{2/3}$)O$_3$–PbTiO$_3$ [49].

The Sm$^{3+}$ (samarium) ion exhibits characteristic luminescence arising from intra-4f electronic transitions, typical of trivalent lanthanide ions. Upon excitation, often into higher-energy 4f levels or via charge-transfer bands, non-radiative relaxation rapidly populates the $^4G_{5/2}$ excited state. From this level, radiative transitions to various sub-levels of the $^6H_J$ ground multiplet produce sharp emission lines in the visible and near-infrared (NIR) regions. Prominent visible emissions include the $^4G_{5/2} \rightarrow {}^6H_{5/2}$ transition around 570 nm (orange-red), $^4G_{5/2} \rightarrow {}^6H_{7/2}$ around 600 nm (red), and $^4G_{5/2} \rightarrow {}^6H_{9/2}$ near 650 nm (deep red) (**Figure 7**) [51]. These f-f transitions are formally parity-forbidden, but their intensity is enhanced through mixing with opposite-parity states and asymmetry in the local crystal field. The 4f orbitals are well shielded by the outer 5s and 5p electrons, making the resulting emission bands narrow and relatively insensitive to the host matrix. Sm$^{3+}$ ions exhibit a unique energy structure due to the interaction of their 4f-electrons with the crystal field, leading to both singlet and triplet states. The sharp emission lines from these transitions, particularly those in the red-orange region, are highly valued for their colour purity. Due to its strong red-orange emission and long luminescence lifetime, Sm$^{3+}$ is widely used in phosphors for lighting [52], lasers [53], and optoelectronic applications [54].

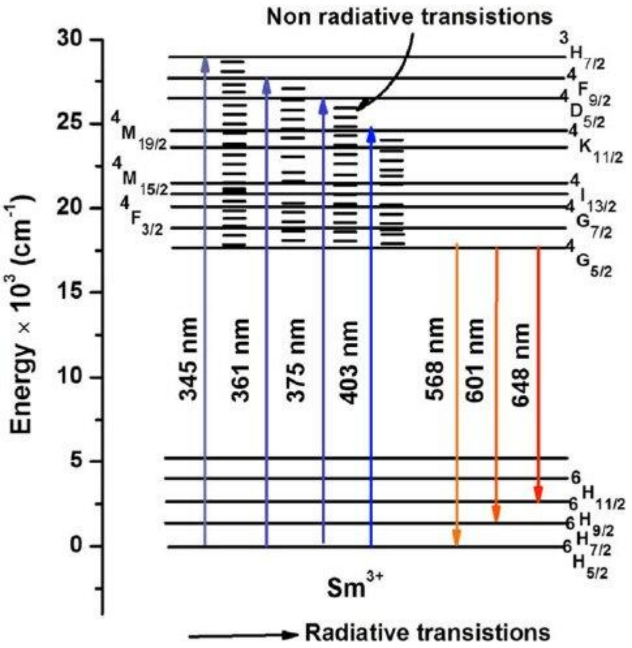

**Figure 7.** $Sm^{3+}$ energy level diagram in Sm-doped $NaCaBO_3$ [51].

The energy level structure of $Tb^{3+}$ (terbium(III)) ions is governed by their $4f^8$ electronic configuration, which results in a multitude of electronic states due to the splitting of the 4f orbitals under the influence of the crystal field and spin-orbit coupling. These 4f orbitals are well shielded by the filled $5s^2$ and $5p^6$ subshells, leading to relatively minor perturbations from the surrounding environment and, consequently, sharp intra-configurational 4f-4f transitions. The most prominent luminescent emission from $Tb^{3+}$ arises from the $^5D_4$ excited state to various lower-lying $^7F_J$ (J = 6-0) levels, with the $^5D_4 \rightarrow {}^7F_5$ transition at approximately 545 nm being responsible for the characteristic green emission (**Figure 8**). This transition is an electric dipole forbidden in free ions but becomes partially allowed in solid-state hosts or coordination environments due to the mixing of opposite parity states [55].

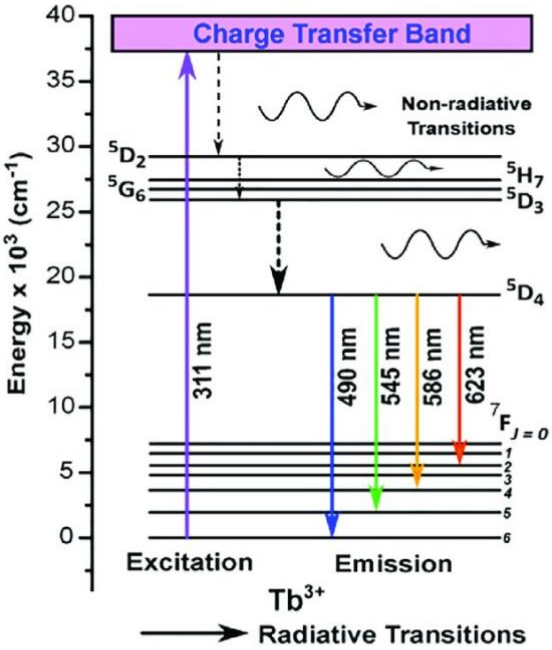

**Figure 8.** $Tb^{3+}$ energy level diagram in Tb-doped $LiSrVO_4$ [55].

Excitation of $Tb^{3+}$ can occur either directly through f-f absorption bands or indirectly via energy transfer from a sensitiser, such as a ligand in a coordination complex or a host lattice component in phosphor materials. The latter pathway often results in more efficient luminescence due to the relatively low absorption cross-section of the 4f orbitals. The radiative decay from the $^5D_4$ state is typically long-lived, with lifetimes ranging from hundreds of microseconds to several milliseconds, depending on the host matrix and non-radiative deactivation pathways. Owing to its sharp emission lines, high colour purity, and long luminescence lifetime, $Tb^{3+}$ is extensively employed in applications such as solid-state lighting, display technologies [12,23], and scintillators [56].

## 1.2 Germanates

Germanates are a class of inorganic compounds containing the germanate anion, typically derived from germanium in its +4 oxidation state. Structurally, they are closely related to silicates, as germanium and silicon share similar chemical properties and coordination preferences. Germanates often form complex three-dimensional frameworks built from $GeO_4$ tetrahedra, and in some cases, $GeO_6$ octahedra, depending on the pressure, temperature, and composition of the system [57,58]. These compounds exhibit a wide range of crystal structures and are of interest for their potential applications in optics, electronics, and materials science [59]. Due to the larger ionic radius of $Ge^{4+}$ compared to $Si^{4+}$, germanates can stabilise unique structural motifs not typically observed in silicates, making them valuable for studying structure-property relationships in crystalline materials [57].

Germanates are synthesised using various methods, most commonly through solid-state reactions [20,36], the citrate method [58], or single-crystal growth [26,30], depending on the desired phase, morphology, and application. Among these, solid-state reactions remain the most widely used approach due to their simplicity, scalability, and suitability for producing bulk polycrystalline materials. The citrate method, a solution-based route, provides good chemical homogeneity and is particularly useful for synthesising nanoscale or doped germanates with uniform elemental distribution. Single-crystal growth methods, such as flux or hydrothermal-assisted growth, are employed when high structural quality is required, particularly in optical and electronic applications. The choice of method, along with parameters like precursors, temperature, and processing time, plays a crucial role in determining the material's final structure and properties.

Doping germanates with aliovalent or isovalent cations is a common strategy to tailor their physical properties for specific applications. Dopants such as rare-earth ions (e.g., $Eu^{3+}$ [24], $Tb^{3+}$ [60]) or transition metals (e.g., $Mn^{2+}$ [61]) can be introduced into the structure to modify optical, luminescent, magnetic, or electrical characteristics. For instance, rare-earth-doped germanates are of particular interest for photonic and phosphor applications due to their efficient luminescence and thermal stability [23].

### 1.2.1 $LiYGeO_4$

$LiYGeO_4$ crystallizes in the orthorhombic phase, with the space group Pnma (62), which defines the symmetry and structural arrangement of the material. The crystal structure consists of a network of interconnected polyhedral units: [$GeO_4$] tetrahedra and [$LiO_6$] and [$YO_6$] octahedra (**Figure 9**) [17]. The $Ge^{4+}$ ions are four-coordinated and occupy tetrahedral sites, where they are surrounded by four oxygen atoms forming the [$GeO_4$] tetrahedra. In contrast, both $Li^+$ and $Y^{3+}$ ions are six-coordinated, located at the centres of the octahedra, and coordinated to six oxygen atoms, forming the [$LiO_6$] and [$YO_6$] octahedra, respectively. These octahedra and tetrahedra are linked together by bridging oxygen atoms, creating a well-structured three-dimensional framework. The [$LiO_6$] octahedra form chains along the b axis, with one octahedron alternating edge-to-edge with the [$GeO_4$] tetrahedra from an adjacent chain, leading to the formation of layers that run parallel to the (100) plane. The [$YO_6$] octahedra are positioned between these chains, acting as layers separating the [$LiO_6$]–[$GeO_4$] chain network. This arrangement contributes to the unique structural features of $LiYGeO_4$, giving it a robust network that influences its physical and optical properties [15].

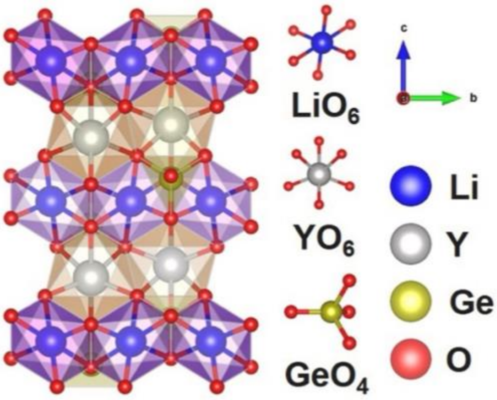

**Figure 9.** Crystal structure diagram of $LiYGeO_4$ [17].

Numerous studies have explored the luminescence properties of $LiYGeO_4$ when doped with different activator ions. One of the most notable developments is the creation of $LiYGeO_4:Bi^{3+}$, which exhibits strong UVA persistent luminescence peaking at 350 nm. After being excited with a 254 nm UV lamp, $LiYGeO_4:Bi^{3+}$ demonstrates an exceptional UVA PerL duration of over 300 hours, a remarkable feature for applications requiring long-lasting afterglow. Additionally, $LiYGeO_4:Bi^{3+}$ showcases excellent photostimulated UVA PerL capabilities even after short-term illumination with red or NIR light, significantly prolonging the UVA PerL time and opening the door to new possibilities in light-emitting applications that require extended afterglow durations [7].

Moreover, $LiYGeO_4:Tb^{3+}$ phosphors, synthesized using a high-temperature solid-phase method, exhibit strong green luminescence under near-UV and blue light excitation, attributed to the $^5D_4 \rightarrow {}^7F_5$ transition of $Tb^{3+}$. These materials also exhibit remarkable long afterglow properties, making them ideal for applications where both fluorescence and afterglow are needed [15]. The $LiYGeO_4:Tb^{3+}$ phosphor is tunable, with its photoluminescence and PerL colours adjustable in real time by varying the $Tb^{3+}$ doping concentration. At lower concentrations, the phosphor emits blue light, which gradually shifts to green as the $Tb^{3+}$ concentration increases. Additionally, $LiYGeO_4:Tb^{3+}$ demonstrates temperature-dependent luminescence, enabling colour tuning from blue to green under varying temperature conditions. This stability and tunability in both PL and PerL properties position $LiYGeO_4:Tb^{3+}$ as a promising candidate for advanced applications such as anti-counterfeiting measures and display technologies [14].

Furthermore, $LiYGeO_4:Eu^{3+}$ phosphors have been developed to emit intense red PerL with a duration of over 21 hours. With low doping concentrations of $Eu^{3+}$, these materials exhibit high intensity red afterglow, expanding the range of available persistent luminescent materials [8]. The unique combination of long-lasting luminescence and stability across different doping schemes and excitation conditions highlights $LiYGeO_4$ versatility as a host material for various activators. These advancements make $LiYGeO_4$-based phosphors highly suitable for applications in information storage [17], high-frequency communication [62], and other innovative technologies [10] where long afterglow, tunable luminescence, and excellent chemical stability are required.

### 1.2.2 $NaYGeO_4$

$NaYGeO_4$ is an orthorhombic germanate compound that adopts an olivine-type crystal structure, characterised by a three-dimensional framework of interconnected polyhedra. It crystallises in the Pnma space group (no. 62), where the $Na^+$ and $Y^{3+}$ ions are situated in distinct coordination environments and occupy specific Wyckoff positions within the lattice (**Figure 10**) [63]. $Na^+$ resides in a centrosymmetric 4c site ($C_i$ symmetry) while $Y^{3+}$ occupies a 4c site of $C_s$ symmetry, and both cations are six-coordinated by oxygen atoms, forming $NaO_6$ and $YO_6$ octahedra. In contrast, $Ge^{4+}$ adopts a fourfold coordination, forming $GeO_4$ tetrahedra. The overall structure is composed of these octahedral and tetrahedral units connected by shared edges and corners, contributing to the compound's structural integrity [58]. The spatial arrangement of the polyhedra results in a robust lattice that supports ion substitution and doping, making $NaYGeO_4$ a promising host material for photoluminescent applications [21,24]. The distinct symmetry environments of $Na^+$ and $Y^{3+}$ also enable site-specific activator incorporation, which can influence luminescence properties depending on the dopant and coordination environment [20].

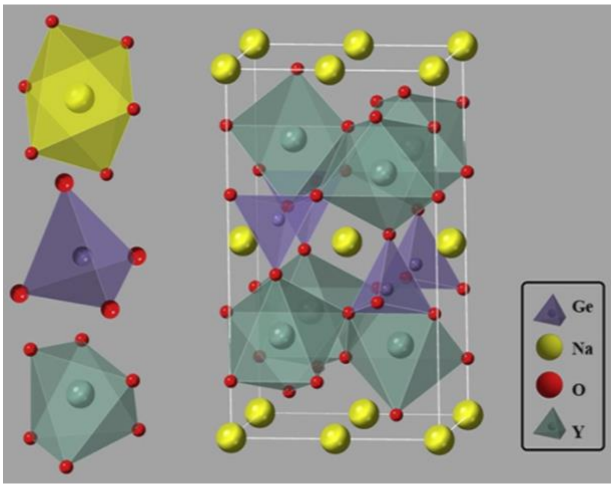

**Figure 10.** Crystal structure diagram of $NaYGeO_4$ [63].

$NaYGeO_4$ has emerged as a versatile host material for the development of colour tunable phosphors through doping with various rare-earth and transition metal ions. When doped with $Bi^{3+}$, $Tb^{3+}$ or $Eu^{3+}$, the material exhibits distinct emissions – blue, green and red, respectively – under UV light excitation. The luminescence can be precisely tuned by adjusting the dopant concentrations. For example, increasing the concentration of $Tb^{3+}$ in $Bi^{3+}/Tb^{3+}$ co-doped $NaYGeO_4$ results in a shift in emission from cyan to cyan-green, while increasing $Eu^{3+}$ in $Bi^{3+}/Eu^{3+}$ samples change the emission from blue to purple-red. A balanced white light emission can be achieved by co-doping $NaYGeO_4$ with $Bi^{3+}$ (0.04), $Tb^{3+}$ (0.01) and $Eu^{3+}$ (0.01–0.03) [20]. Furthermore, co-doping with $Tm^{3+}$, $Tb^{3+}$ and $Eu^{3+}$ enables simultaneous blue, green and red emissions, which can be adjusted to produce white light by optimising the ratios of $Tm^{3+}$ (0.03), $Eu^{3+}$ (0.07) and $Tb^{3+}$ (0.12) [23]. Notably, in $NaYGeO_4$:$Tb^{3+}$, a colour shift from red to green is observed with increasing $Tb^{3+}$ content, attributed to cross-relaxation between neighbouring $Tb^{3+}$ ions – a feature that makes it suitable for multi-colour luminescent anti-counterfeiting applications [63]. The host itself exhibits a broad self-activated emission band, and when doped with $Eu^{3+}$, $Sm^{3+}$ or $Dy^{3+}$, the emission spectra display both – host and dopant specific features, indicating efficient host-to-activator energy transfer [22]. In particular, $Eu^{3+}$-doped $NaYGeO_4$ phosphors show strong red emission at 613 nm, high internal quantum efficiency (up to 65%), and excellent thermal stability, maintaining over 80% of their emission intensity at elevated temperatures [24]. These characteristics position NaYGeO$_4$-based phosphors as promising candidates for white LEDs, UV-excited displays and optical data storage technologies.

### 1.2.3 LiAlGeO$_4$

LiAlGeO$_4$, also known as lithium alumogermanate or germanium eucryptite, crystallises in the phenakite-type structure with a centrosymmetric space group $R\bar{3}$ (no. 148) and unit cell parameters a = 13.7683(9) Å and c = 9.1919(5) Å (**Figure 11**). This compound is isostructural with the low-temperature phase of $\alpha$-LiAlSiO$_4$, a naturally occurring mineral known as eucryptite. The crystal framework is composed of interconnected cation–oxygen tetrahedra forming a three-dimensional network with columns aligned along the crystallographic c-axis. Within this framework, lithium ions occupy the larger tetrahedral T1 sites, while aluminium and germanium ions are statistically distributed over the smaller T2 and T3 sites. The lack of polymorphic transitions up to the melting point highlights the structural stability of LiAlGeO$_4$, reinforcing its significance as a stable host for doped systems and its value in the study of phenakite-like germanates [26].

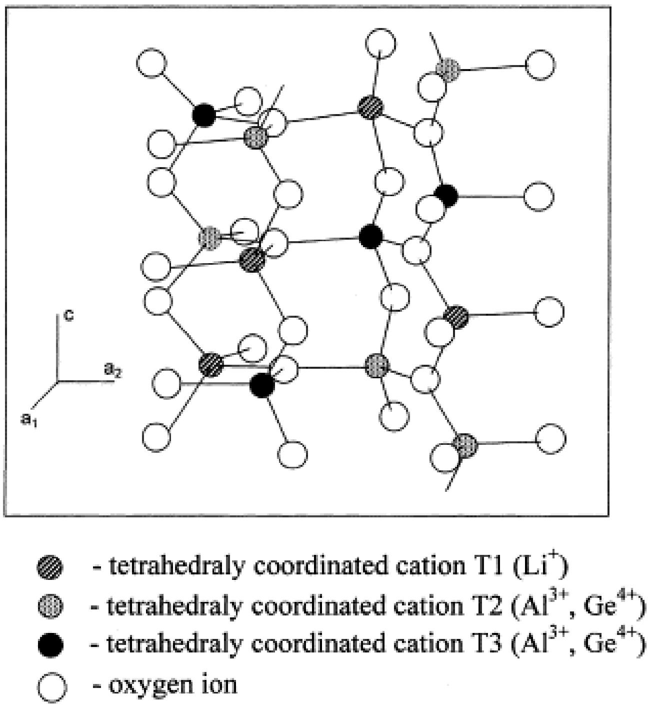

**Figure 11.** Crystal structure diagram of LiAlGeO$_4$ [26].

LiAlGeO$_4$ offers a stable framework for doping with various ions, enabling enhanced optical properties. LiAlGeO$_4$, when doped with Cr$^{4+}$ ions, shows a strong potential for nonlinear optical applications due to its distinct absorption and luminescence properties. The absorption spectrum exhibits broad, intense bands corresponding to tetrahedron-coordinated Cr$^{4+}$ ions. The luminescence decay follows a single-exponential pattern, with the excited state lifetime of Cr$^{4+}$ increasing from 10 μs at room temperature to 70 μs at 77 K. These characteristics reinforce the material's suitability as a stable host for doped systems, particularly in photonics and laser technologies, underscoring its relevance for the study of phenakite-like germanates [26].

### 1.2.4 NaAlGeO4

Sodium aluminium germanate ($NaAlGeO_4$) crystallises in a monoclinic crystal system and belongs to the space group $P2_1/n$, which corresponds to space group No. 14 in the International Tables for Crystallography. The crystal structure is composed of $Al^{3+}$ and $Ge^{4+}$ cations, each coordinated tetrahedrally by oxygen atoms, forming a three-dimensional framework. Sodium ions ($Na^+$) occupy the interstitial spaces within this framework and are coordinated octahedrally, contributing to the overall structural stability of the lattice (**Figure 12**). The unit cell parameters of $NaAlGeO_4$ are as follows: a = 8.783 Å, b = 15.432 Å, and c = 8.252 Å. The unit cell angles are $\alpha = 90.00°$, $\beta = 90.00°$, and $\gamma = 90.09°$, indicating a structure that is nearly orthorhombic in geometry but with a slight distortion that justifies its classification as monoclinic [32].

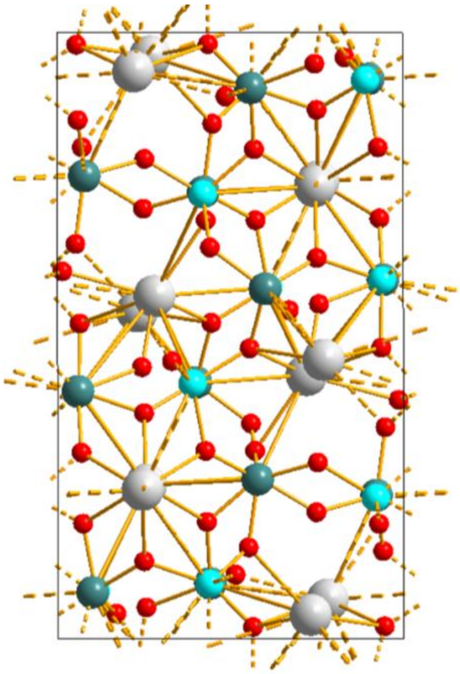

**Figure 12.** The crystal structure of $NaAlGeO_4$. Oxygen anions are shown in red, $Na^+$ cations in grey, $Al^{3+}$ in green, and $Ge^{4+}$ in light blue [32].

In terms of ionic dimensions, the radii of the constituent cations are $Na^+$ – 118 pm, $Al^{3+}$ – 39 pm, and $Ge^{4+}$ – 39 pm [64]. The close similarity in ionic radii between $Al^{3+}$ and $Ge^{4+}$ facilitates the formation of a regular tetrahedral network, while the significantly larger $Na^+$ ion is well-suited to the octahedral voids within the framework. This combination of coordination environments and ionic sizes plays a critical role in determining the overall crystal packing, stability, and potential properties of the material.

In this study, $Na_{1-x}AlGe_{1-0.5x}GeO_4$ is doped with a range of rare-earth metal ions and bismuth ($Bi^{3+}$, ionic radius 103 pm). The dopants include dysprosium ($Dy^{3+}$, ionic radius 91 pm), europium ($Eu^{3+}$, ionic radius 95 pm), praseodymium ($Pr^{3+}$, ionic radius 99 pm), samarium ($Sm^{3+}$, ionic radius 99 pm), and terbium ($Tb^{3+}$, ionic radius 92 pm) [64]. These ions are strategically introduced to partially substitute for $Na^+$ and $Ge^{4+}$ cations within the crystal structure of $NaAlGeO_4$, as their ionic radii are comparable to those of the host ions, making them ideal candidates for substitution without causing significant disruption to the lattice.

# 2. EXPERIMENTAL METHODOLOGY

## 2.1 Reagents

The following materials were used for the syntheses performed in this study: sodium carbonate ($Na_2CO_3$, 99.5%, Alfa Aesar), aluminium oxide ($Al_2O_3$, 99+%, Alfa Aesar), germanium(IV) oxide ($GeO_2$, 99.998%, Sigma-Aldrich), bismuth(III) oxide ($Bi_2O_3$, 99%, Alfa Aesar), dysprosium(III) oxide ($Dy_2O_3$, 99.9%, Sigma-Aldrich), europium(III) oxide ($Eu_2O_3$, 99.99%, Alfa Aesar), praseodymium(III, IV) oxide ($Pr_6O_{11}$, 99.9%, Sigma-Aldrich), samarium(III) oxide ($Sm_2O_3$, 99.9%, Sigma-Aldrich), terbium(III, IV) oxide ($Tb_4O_7$, 99.9%, Sigma-Aldrich).

## 2.2 Equipment

Analytical balance: manufacturer Kern, MAX 220 g, MIN 10 mg, e = 1 mg, d = 0.1 mg, 12V/1250 mA.

High-temperature muffle furnace: manufacturer Nabertherm, 400 V, 5.2 kW, 50/60 Hz.

Diffractometer: manufacturer Rigaku, model MiniFlex II, Bragg-Brentano geometry (θ/2θ). Cu $K_\alpha$ ($\lambda$ = 1.5406 Å) radiation was used, with a scanning speed of 10°/min (step size 0.01°), and data were collected in the 2θ range from 10° to 70° at room temperature.

Spectrometer: manufacturer Edinburgh Instruments, model FLS980, equipped with a 450 W Xe arc discharge lamp, Hamamatsu R928P photomultiplier, and mirror optics for powder analysis. Measurements were taken with a step size of 0.5 nm and a signal acquisition time of 0.20 seconds. All emission spectra were corrected using a file provided by Edinburgh Instruments. Quantum efficiencies were calculated by measuring the emission spectra of the samples inside a Teflon coated integrating sphere, using $BaSO_4$ as a reference.

## 2.3 Synthesis of $NaAlGeO_4$

### 2.3.1 $NaAlGeO_4$ synthesis via solid-state reactions

Initially, the necessary quantities of starting reagents were calculated to synthesize 1 g of the compound. The reagents were then precisely weighed using an analytical balance and finely ground in an agate mortar with a small amount of acetone to achieve a homogeneous mixture. The prepared mixture was transferred to a crucible and heated at 1000°C for 4 hours. After cooling, the synthesized product was ground again in an agate mortar to ensure uniformity.

### 2.3.2 $NaAlGeO_4$ doping

$NaAlGeO_4$ was doped with bismuth, dysprosium, europium, praseodymium, samarium, and terbium. The respective amounts of dopants introduced into the initial reagent mixture were:

- Bismuth: 0.1%, 0.2%, 0.3%, 0.4%, 0.5%, 0.7%, 1%, 2%, 4%.
- Dysprosium: 0.1%, 0.5%, 1%, 1.5%, 2%, 4%, 8%.
- Europium: 0.1%, 0.25%, 0.5%, 0.75%, 1%, 2%, 4%, 8%.
- Praseodymium: 0.1%, 0.25%, 0.5%, 0.75%, 1%, 2%, 4%, 8%.
- Samarium: 0.1%, 0.25%, 0.5%, 0.75%, 1%, 2%, 4%, 8%.

- Terbium: 0.1%, 0.25%, 0.5%, 0.75%, 1%, 2%, 4%, 8%.

The doping process involved substituting part of the $Na^+$ and $Ge^{4+}$ ions with dopant ions in the ratio $Na_{1-x}AlGe_{1-0.5x}GeO_4$, where $x$ represents the dopant concentration. This substitution is expected to alter the sodium coordination environment due to the similar ionic radii of the dopant and $Na^+$, while simultaneously reducing the $Ge^{4+}$ content to maintain overall charge neutrality. Among the various charge-compensation strategies examined in earlier studies—namely $NaAl_{1-x}GeO_4$, $Na_{1-x}AlGe_{1-0.5x}O_4$, $Na_{1-x}AlGeO_4$ and $Na_{1-3x}AlGeO_4$—the $Na_{1-x}AlGe_{1-0.5x}GeO_4$ composition yielded the most favourable results. The synthesis procedure then followed the steps described in section **2.3.1**.

### 2.3.3 PL emission decay analysis

Photoluminescence emission decay was measured using the same Edinburgh Instruments spectrometer. The obtained decay curves were interpreted using a biexponential decay function [65]:

$$\boldsymbol{I(t) = y_0 + A_1 e^{-t/\tau_1} + A_2 e^{-t/\tau_2}} \qquad \textbf{(1)}$$

where $I(t)$ – represents the luminescence intensity as a function of time $t$, $y_0$ is the background signal, $A_1$ and $A_2$ are pre-exponential factors, and $\tau$ is the photoluminescence decay time.

The average decay lifetimes were calculated using the following equation [65]:

$$\boldsymbol{\tau_{avg} = \frac{(\tau_1 f_1 + \tau_2 f_2)}{100\%}} \qquad \textbf{(2)}$$

where $\tau$ represents the photoluminescence decay time and $f$ is the weighting factor of the decay time.

# 3. RESULTS AND DISCUSSION

## 3.1 $Bi^{3+}$ doped $NaAlGeO_4$: XRD, photoluminescence spectra, CIE 1931 diagram, QY

The X-ray diffraction patterns of $NaAlGeO_4$ doped with different concentrations of $Bi^{3+}$ ions (ranging from 0.1% to 4%) are presented in **Figure 13**. The undoped $NaAlGeO_4$ sample exhibits diffraction peaks that are in excellent agreement with the standard pattern of $NaAlGeO_4$ (PDF#01–078–1172), confirming the phase purity of the synthesized material.

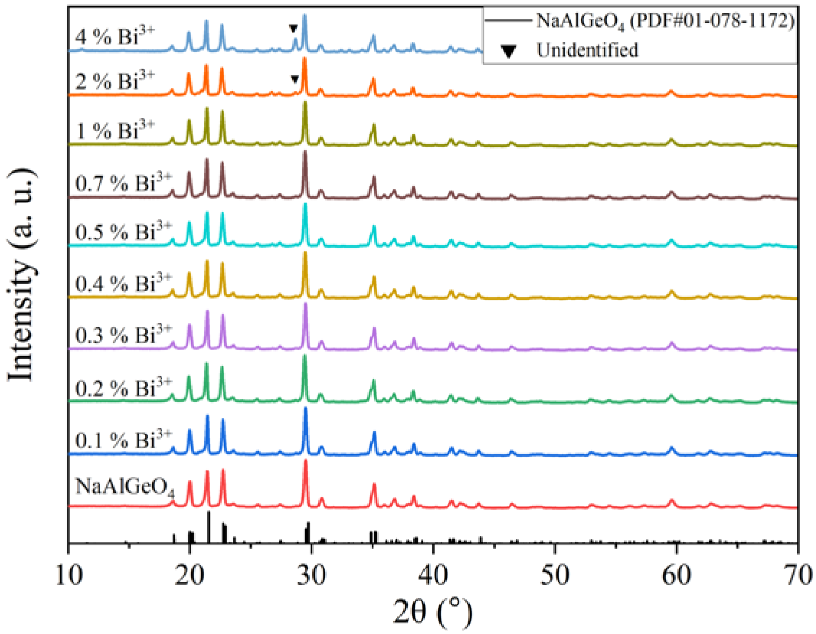

**Figure 13.** XRD patterns of $NaAlGeO_4$ samples doped with different concentrations of $Bi^{3+}$ ions. Black bars represent standard diffraction peaks of $NaAlGeO_4$ (PDF#01–078–1172).

Upon doping with $Bi^{3+}$, all samples retain the primary diffraction peaks corresponding to $NaAlGeO_4$, indicating that the crystal structure remains largely intact even at the highest doping concentration of 4%. This suggests that $Bi^{3+}$ ions are successfully incorporated into the $NaAlGeO_4$ lattice without causing significant structural distortion.

Notably, additional diffraction peaks, marked with black triangles, appear in the patterns for samples doped with 2% and 4% $Bi^{3+}$. These peaks are unidentified and may correspond to secondary phases or impurities formed. The intensity of these unidentified peaks increases with higher $Bi^{3+}$ concentration, suggesting the onset of phase segregation or crystallization of Bi-containing secondary phases. In conclusion, the XRD analysis confirms that $NaAlGeO_4$ can accommodate $Bi^{3+}$ doping up to 1% without notable secondary phase formation.

The photoluminescence properties of $NaAlGeO_4$ doped with various concentrations of $Bi^{3+}$ ions were investigated through excitation and emission spectra, as shown in **Figure 14**. The excitation spectra, monitored at an emission wavelength of 420 nm, display a broad excitation band centred around 300 nm, corresponding to the $^1S_0 \rightarrow {}^3P_1$ transition of $Bi^{3+}$ ions. Based on the research findings of P. Shao et al., the excitation peak of $Bi^{3+}$-doped $LiYGeO_4$ phosphor is at a wavelength of 303 nm [10], as also reported by J. Shi et al [35]. For $NaYGeO_4$:Bi, the excitation peak is observed at 328 nm [20].

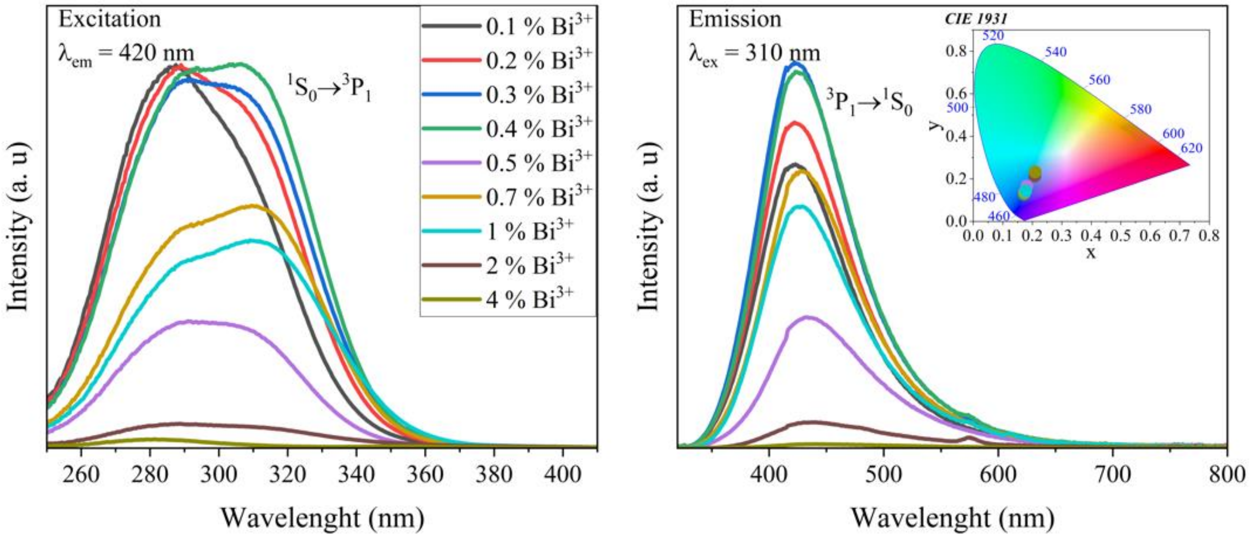

**Figure 14.** Photoluminescence excitation ($\lambda_{em}$ = 420 nm) and emission ($\lambda_{ex}$ = 310 nm) spectra of $NaAlGeO_4$:Bi samples. Inset shows CIE 1931 chromaticity diagram.

The excitation intensity remains similar for $Bi^{3+}$ concentrations between 0.1% and 0.4%. Beyond this range, further increases in $Bi^{3+}$ concentration result in a decrease in intensity. This behaviour indicates the occurrence of concentration quenching effects beyond the optimal doping level, likely due to energy transfer processes between closely spaced $Bi^{3+}$ ions leading to non-radiative relaxation [35].

The emission spectra, measured at an excitation wavelength of 310 nm, exhibit a strong emission peak around 420 nm, attributed to the $^3P_1 \rightarrow {}^1S_0$ transition of $Bi^{3+}$. Comparable to the excitation spectra, the emission intensity peaks at low doping concentrations and is weakest in samples with 2% and 4% doping. Consistent with the findings reported in the article mentioned earlier, a similar pattern is observed in $LiYGeO_4$ samples doped with $Bi^{3+}$, where an increase in dopant ion concentration from 0.5% to 1.75% leads to a decrease in emission intensity [35].

The CIE 1931 chromaticity diagram inset in **Figure 14** illustrates the emission colour coordinates of the samples, indicating a shift towards blue emission with increasing $Bi^{3+}$ concentration. The coordinates cluster around the blue region, confirming the potential of $NaAlGeO_4$:$Bi^{3+}$ as an efficient blue emitting phosphor.

The quantum yields (QY) of $NaAlGeO_4$ samples doped with varying concentrations of $Bi^{3+}$ ions are summarized in **Table 2.** The highest quantum yield is observed at 0.2% $Bi^{3+}$ doping, achieving 5.80%. This is followed closely by 0.3% and 0.1% $Bi^{3+}$ doped samples, with quantum yields of 5.45% and 5.38%, respectively. The trend indicates that optimal quantum yield is achieved at lower $Bi^{3+}$ concentrations. When the $Bi^{3+}$ concentration exceeds 0.4%, the quantum yield decreases significantly. This decline continues with higher doping levels, reaching minimum values of 0.04% at 2% $Bi^{3+}$ and 0.02% at 4% $Bi^{3+}$ samples.

**Table 2.** Quantum yields of doped $Na_{1-x}AlGe_{1-0.5x}O_4$ samples, where x is $Bi^{3+}$.

| Sample | Quantum yield, % |
|---|---|
| 0.1% $Bi^{3+}$ | 5.38 |
| 0.2% $Bi^{3+}$ | 5.80 |

| | |
|---|---|
| 0.3% $Bi^{3+}$ | 5.45 |
| 0.4% $Bi^{3+}$ | 4.94 |
| 0.5% $Bi^{3+}$ | 1.50 |
| 0.7% $Bi^{3+}$ | 3.16 |
| 1% $Bi^{3+}$ | 2.96 |
| 2% $Bi^{3+}$ | 0.04 |
| 4% $Bi^{3+}$ | 0.02 |

The reduction in quantum yield at higher doping concentrations can be attributed to concentration quenching effects, where increased $Bi^{3+}$ ion proximity facilitates non-radiative energy transfer pathways, reducing luminescence efficiency. This behaviour aligns with the observed emission intensity trends, confirming the adverse impact of excessive $Bi^{3+}$ doping on luminescence performance.

### 3.2 $Dy^{3+}$ doped $NaAlGeO_4$: XRD, photoluminescence spectra, CIE 1931 diagram, decay lifetimes, QY

The XRD patterns of $NaAlGeO_4$ doped with different concentrations of $Dy^{3+}$ ions (ranging from 0.1% to 8%) are shown in **Figure 15**. Doping with $Dy^{3+}$ does not significantly alter the primary diffraction peaks of $NaAlGeO_4$, indicating that the crystal structure is maintained even at higher doping levels up to 8%. This suggests that $Dy^{3+}$ ions are incorporated into the $NaAlGeO_4$ lattice successfully. However, unidentified peaks, marked with black triangles, emerge in samples with $Dy^{3+}$ concentrations of 1.5% and higher, indicating the formation of secondary phases or impurities. The intensity of these peaks increases with higher $Dy^{3+}$ doping levels, supporting the possibility of phase segregation or secondary phase crystallization. Despite this, the well-defined nature of the main diffraction peaks suggests that the crystalline structure of $NaAlGeO_4$ remains largely intact.

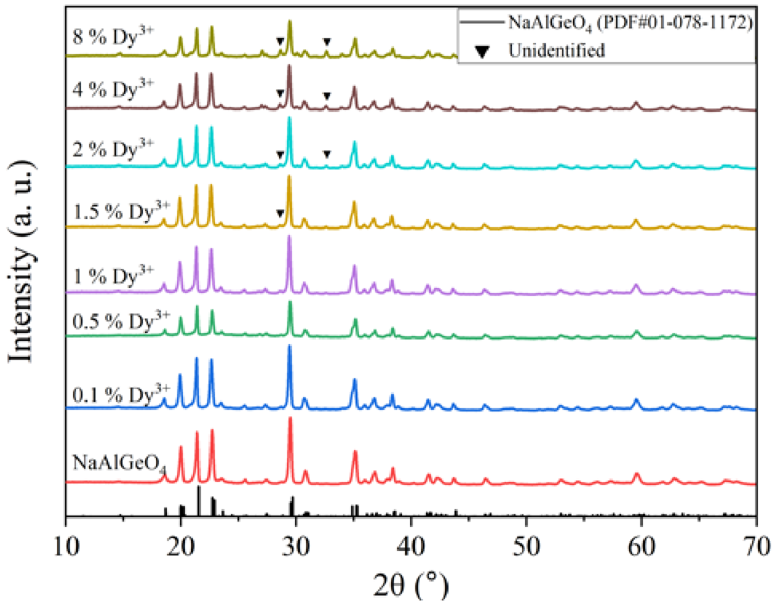

**Figure 15.** XRD patterns of $NaAlGeO_4$ samples doped with different concentrations of $Dy^{3+}$ ions. Black bars represent standard diffraction peaks of $NaAlGeO_4$.

The photoluminescence behaviour of $NaAlGeO_4$ doped with varying concentrations of $Dy^{3+}$ ions was thoroughly examined through excitation and emission spectra, as illustrated in **Figure 16**. The excitation spectra, monitored at an emission wavelength of 574 nm, reveal distinct absorption bands corresponding to the characteristic 4f-4f transitions of $Dy^{3+}$ ions. These transitions include $^6H_{15/2} \rightarrow {}^4G_{9/2}$, $^6H_{15/2} \rightarrow {}^4I_{11/2}$, and $^6H_{15/2} \rightarrow {}^6P_{7/2}$, indicating efficient energy absorption within the UV to near-visible range. Under 386 nm excitation, the emission spectra display two prominent peaks at 486 nm and 574 nm, corresponding to the $^4F_{9/2} \rightarrow {}^6H_{15/2}$ (blue emission) and $^4F_{9/2} \rightarrow {}^6H_{13/2}$ (yellow emission) transitions, respectively. Consistent with this, J. Zhang's study on NaYGeO4:Dy reported that the $^4F_{9/2} \rightarrow {}^6H_{13/2}$ transition at 577 nm has the strongest emission [22]. The emission intensity varies with $Dy^{3+}$ concentration, peaking at 0.1% doping, after which intensity decreases due to concentration related non-radiative energy transfer processes. The inset of the CIE 1931 chromaticity diagram shows tunable emission colours, with coordinates shifting according to $Dy^{3+}$ concentration, emphasising the material's potential for white-light applications and colour tunable photonic devices.

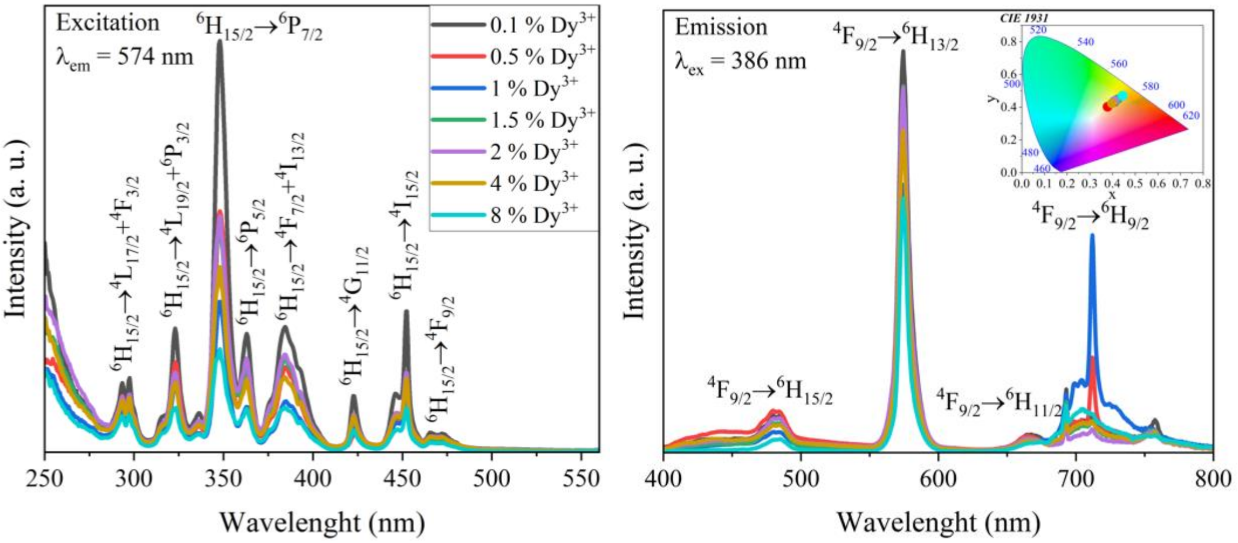

**Figure 16.** Photoluminescence excitation ($\lambda_{em}$ = 574 nm) and emission ($\lambda_{ex}$ = 386 nm) spectra of NaAlGeO4:Dy samples. Inset shows CIE 1931 chromaticity diagram.

The decay kinetics of $Na_{1-x}AlGe_{1-0.5x}O_4:Dy_x$ phosphors exhibit a strong dependence on dopant concentration, with noticeable variations in the average decay time ($\tau_{avg}$) (**Table 3** and **Figure 17**). At the lowest $Dy^{3+}$ concentration (0.1%), the longest decay time of 538.19 μs was observed, indicating efficient radiative recombination. However, as the doping level increased to 0.5% and 1%, $\tau_{avg}$ dropped significantly to 257.60 μs and 215.24 μs, respectively, suggesting the onset of concentration quenching. Interestingly, at higher $Dy^{3+}$ concentrations (1.5%–8%), the decay times exhibited some fluctuation but remained within a narrower range (310.82–326.18 μs), implying a balance between non-radiative losses and energy transfer processes. However, for samples with $Dy^{3+}$ concentrations above 1.5% (**Figure 15**), the presence of impurities may also influence the observed decay behaviour.

**Table 3.** Decay kinetics data for $Na_{1-x}AlGe_{1-0.5x}O_4:Dy_x$ samples.

| Sample | $\tau_1$, $\mu$s | Rel, % | $\tau_2$, $\mu$s | Rel, % | $\tau_{avg}$, $\mu$s |
|---|---|---|---|---|---|
| 0.1% | 179.61 | 25.13 | 658.55 | 74.87 | 538.19 |
| 0.5% | 77.40 | 36.58 | 361.54 | 63.42 | 257.60 |
| 1% | 61.75 | 41.88 | 325.84 | 58.12 | 215.24 |
| 1.5% | 83.64 | 32.81 | 444.61 | 67.19 | 326.18 |
| 2% | 87.69 | 33.96 | 448.28 | 66.04 | 325.59 |
| 4% | 86.29 | 32.98 | 421.31 | 67.02 | 310.82 |
| 8% | 95.03 | 33.67 | 441.46 | 66.33 | 324.82 |

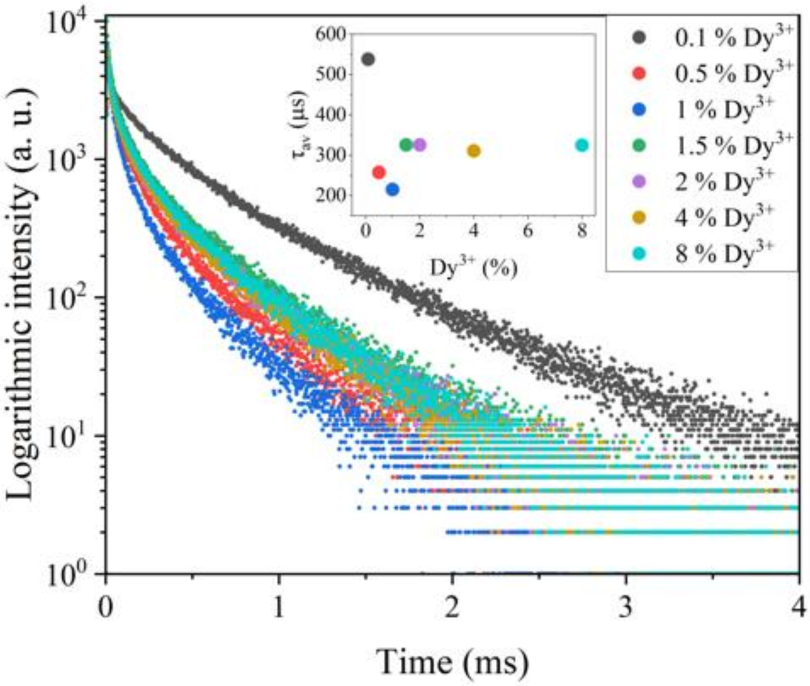

**Figure 17.** Luminescence emission decay times of $NaAlGeO_4$ samples with varying $Dy^{3+}$ concentrations. The inset shows the dependence of average decay lifetimes on $Dy^{3+}$ concentration in the samples.

The quantum yields of Dy-doped $NaAlGeO_4$ samples were investigated to evaluate the effect of varying $Dy^{3+}$ concentrations on the luminescent efficiency (**Table 4**). The data reveals a significant dependence of quantum yield on the $Dy^{3+}$ doping level. At a low doping concentration of 0.1% $Dy^{3+}$, the quantum yield was 1.57%, increasing to a peak of 3.94% at 0.5% $Dy^{3+}$, the highest among the samples tested. Beyond this point, the quantum yield exhibited a fluctuating decline, reaching 1.72% at 1% $Dy^{3+}$, rising slightly to 3.45% at 1.5%, and then decreasing to 2.87% at 2%. At higher doping levels, specifically 4% and 8% $Dy^{3+}$, the quantum yield continued to drop, reaching 1.89% and 1.31%, respectively. This trend suggests that while moderate doping enhances the quantum yield, higher concentrations may lead to non-radiative losses or concentration quenching effects, reducing the overall efficiency [66]. These findings highlight the importance of optimizing $Dy^{3+}$ doping levels for achieving the highest luminescent performance in $NaAlGeO_4$-based materials.

**Table 4.** Quantum yields of doped $Na_{1-x}AlGe_{1-0.5x}O_4$ samples, where x is $Dy^{3+}$.

| Sample | Quantum yield, % |
|---|---|
| 0.1% $Dy^{3+}$ | 1.57 |
| 0.5% $Dy^{3+}$ | 3.94 |
| 1% $Dy^{3+}$ | 1.72 |
| 1.5% $Dy^{3+}$ | 3.45 |
| 2% $Dy^{3+}$ | 2.87 |
| 4% $Dy^{3+}$ | 1.89 |
| 8% $Dy^{3+}$ | 1.31 |

### 3.3 $Eu^{3+}$ doped $NaAlGeO_4$: XRD, photoluminescence spectra, CIE 1931 diagram, decay lifetimes, QY

X-ray diffraction patterns of $NaAlGeO_4$ doped with different $Eu^{3+}$ concentrations (ranging from 0.1% to 8%) confirm the phase purity of the host material at lower doping levels (**Figure 18**). The diffraction peaks of undoped $NaAlGeO_4$ match well with the standard $NaAlGeO_4$ phase (PDF#01–078–1172), indicating the successful synthesis of the material. At doping levels of 4% and 8% $Eu^{3+}$, additional diffraction peaks appear, marked as impurities. These unidentified peaks suggest the formation of secondary phases or segregation of Eu containing compounds due to the limited solubility of $Eu^{3+}$ in the $NaAlGeO_4$ lattice.

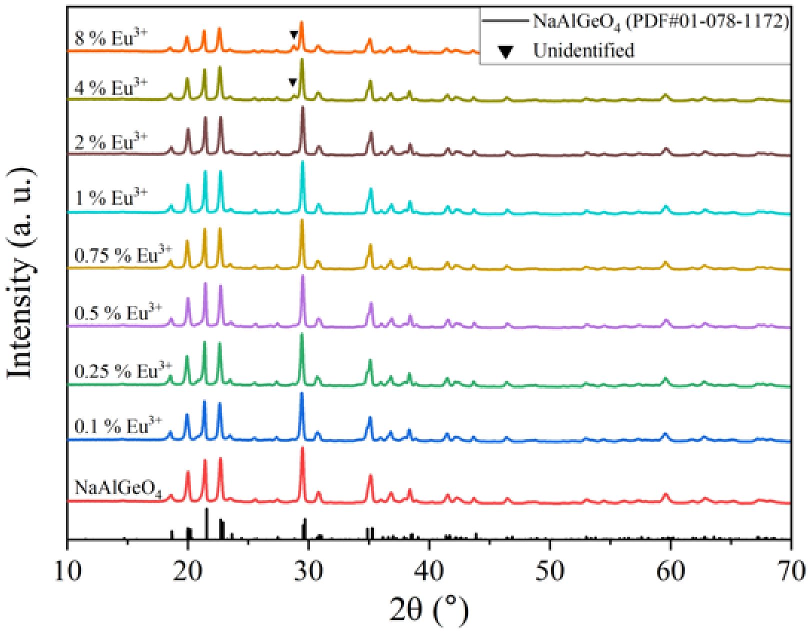

**Figure 18.** XRD patterns of $NaAlGeO_4$ samples doped with different concentrations of $Eu^{3+}$ ions. Black bars represent standard diffraction peaks of $NaAlGeO_4$.

The excitation and emission spectra of $NaAlGeO_4$ doped with $Eu^{3+}$ ions, as illustrated in **Figure 19**, highlight the characteristic 4f-4f transitions of $Eu^{3+}$ and their dependence on dopant concentration. The excitation spectrum, monitored at 611 nm emission, exhibits multiple sharp peaks corresponding to transitions from the ground state $^7F_0$ to higher energy states such as $^5L_6$ (394 nm), $^5D_2$ (464 nm), and $^5D_4$ (362 nm). Among these, the $^7F_0 \rightarrow {}^5L_6$ transition at 394 nm is the most intense, indicating efficient absorption in the near-UV region. A broad absorption band characteristic of the charge transfer (CT) transition of $Eu^{2+}$ is observed in the 270–360 nm range. This band originates from electron transfer between the Eu ion and surrounding oxygen ligands in the host lattice. The broad nature of the CT band, in contrast to the sharp 4f-4f transitions of $Eu^{3+}$, indicates strong 4f-5d orbital coupling and interaction with the host environment.

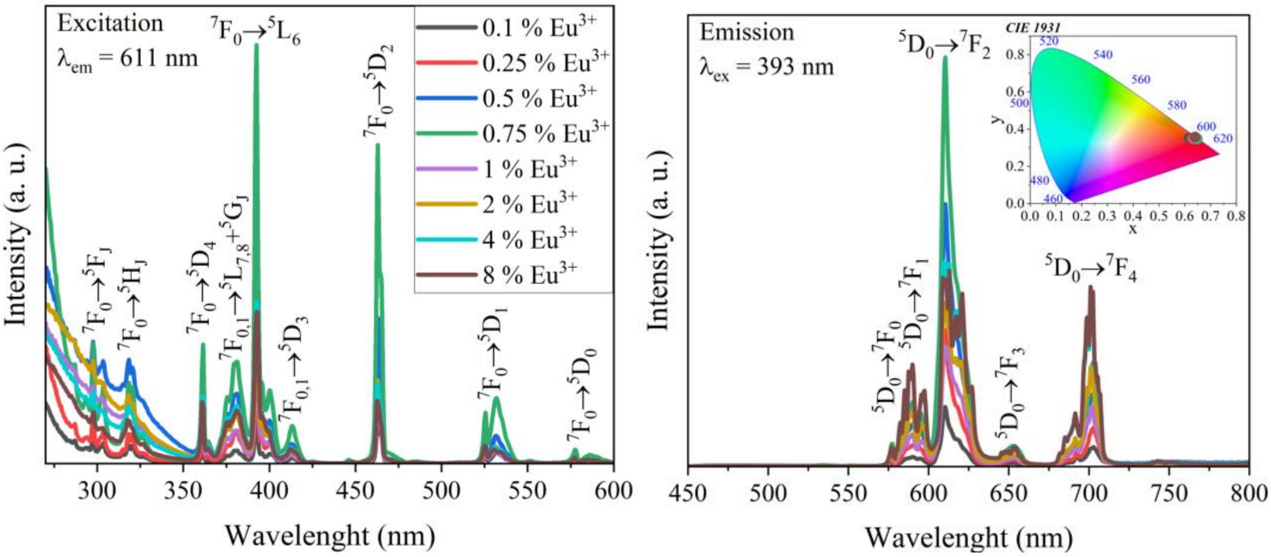

**Figure 19.** Photoluminescence excitation ($\lambda_{em}$ = 611 nm) and emission ($\lambda_{ex}$ = 393 nm) spectra of $NaAlGeO_4$:Eu samples. Inset shows CIE 1931 chromaticity diagram.

Under 393 nm excitation, the emission spectrum reveals a series of characteristic $Eu^{3+}$ transitions. The most intense peak at 611 nm is attributed to the electric dipole transition $^5D_0 \rightarrow {}^7F_2$, which is hypersensitive to the local coordination environment of $Eu^{3+}$ and strongly influenced by the host lattice symmetry. Additional emissions are observed at 590 nm ($^5D_0 \rightarrow {}^7F_1$), which arises from a magnetic dipole transition and remains relatively insensitive to site symmetry, as well as weaker peaks at 650 nm ($^5D_0 \rightarrow {}^7F_3$) and 700 nm ($^5D_0 \rightarrow {}^7F_4$). These findings align with previous studies, which reported the strongest emission peak at 611 nm [8,12] and 613 nm [9] for $LiYGeO_4:Eu^{3+}$, and at 613 nm [21–24] and 617 nm [20] for $NaYGeO_4:Eu^{3+}$. The emission intensity follows a non-linear trend with increasing $Eu^{3+}$ concentration, reaching its maximum at 0.75%. This indicates an optimal doping level at 0.75% $Eu^{3+}$, beyond which concentration quenching effects [24], likely due to non-radiative energy transfer between neighbouring $Eu^{3+}$ ions, reduce the luminescence efficiency.

The CIE 1931 chromaticity diagram (inset in **Figure 19**) confirms a strong red emission, with chromaticity coordinates remaining in the deep red region. These findings highlight $NaAlGeO_4:Eu^{3+}$ as a promising red phosphor material for applications in solid-state lighting and display technologies, particularly for red-emitting phosphor–converted LEDs.

The decay times of $Na_{1-x}AlGe_{1-0.5x}O_4:Eu_x$ phosphors were analysed for various dopant concentrations, revealing a significant dependence of the average decay time ($\tau_{avg}$) on $Eu^{3+}$ content (**Table 5** and **Figure 20**). At low doping levels (0.1%–0.75%), the decay time remained relatively high, with a maximum of 1589.42 µs at 0.25%. However, as the $Eu^{3+}$ concentration increased beyond 1%, a noticeable quenching effect occurred, leading to a sharp decline in $\tau_{avg}$, reaching just 344.72 µs at 8%. This reduction suggests enhanced non-radiative energy transfer and concentration quenching at higher $Eu^{3+}$ levels, influencing the material's luminescence efficiency.

**Table 5.** Decay kinetics data for $Na_{1-x}AlGe_{1-0.5x}O_4:Eu_x$ samples.

| Sample | $\tau_1$, $\mu$s | Rel, % | $\tau_2$, $\mu$s | Rel, % | $\tau_{avg}$, $\mu$s |
|---|---|---|---|---|---|
| 0.1% | 822.09 | 33.83 | 1919.59 | 66.17 | 1548.31 |
| 0.25% | 841.93 | 29.11 | 1896.36 | 70.89 | 1589.42 |
| 0.5% | 388.72 | 17.29 | 1467.67 | 82.71 | 1281.12 |
| 0.75% | 530.22 | 15.52 | 1679.77 | 84.48 | 1501.36 |
| 1% | 160.31 | 22.90 | 1340.44 | 77.10 | 1070.19 |
| 2% | 173.74 | 36.22 | 1315.48 | 63.78 | 901.94 |
| 4% | 187.28 | 61.40 | 1235.50 | 38.60 | 591.89 |
| 8% | 183.18 | 76.71 | 876.77 | 23.29 | 344.72 |

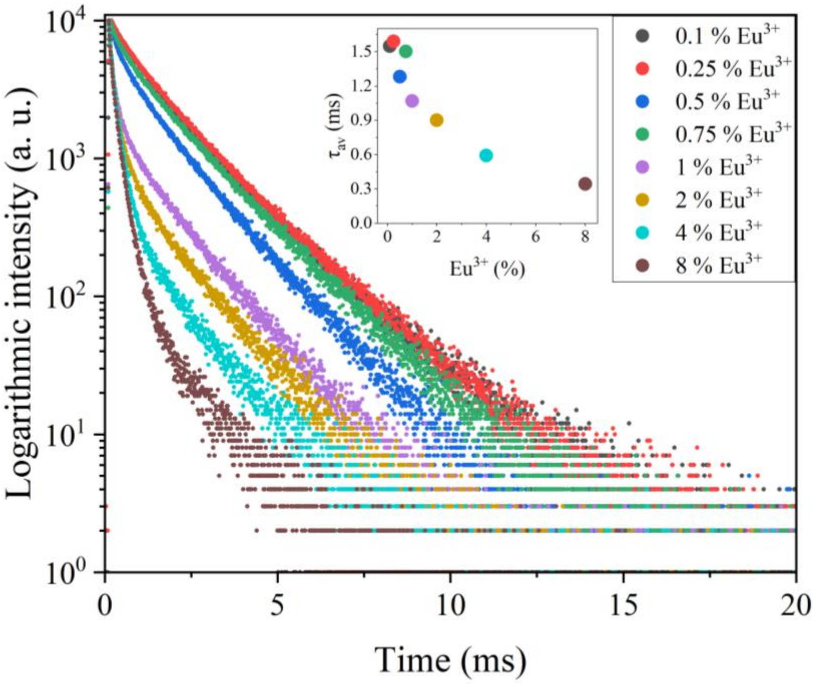

**Figure 20.** Luminescence emission decay times of $NaAlGeO_4$ samples with varying $Eu^{3+}$ concentrations. The inset shows the dependence of average decay lifetimes on $Eu^{3+}$ concentration in the samples.

The quantum yields of $NaAlGeO_4$ samples doped with varying concentrations of $Eu^{3+}$ ions are summarised in **Table 6**. The highest value, 14.27%, is observed at 0.5% $Eu^{3+}$ doping, followed by 10.70% at 0.75%. Beyond this concentration, the quantum yield gradually declines, reaching just 3.13% at 8% doping. The decreasing trend at high $Eu^{3+}$ concentrations suggests that excessive doping leads to non-radiative energy transfer pathways, reducing overall luminescence efficiency. This behaviour aligns with the observed structural analysis (**Figure 18**), where impurities are detected at 4% and 8% $Eu^{3+}$ doping, further impacting the quantum yield.

**Table 6.** Quantum yields of doped $Na_{1-x}AlGe_{1-0.5x}O_4$ samples, where x is $Eu^{3+}$.

| Sample | Quantum yield, % |
|---|---|
| 0.1% $Eu^{3+}$ | 1.93 |
| 0.25% $Eu^{3+}$ | 2.72 |
| 0.5% $Eu^{3+}$ | 14.27 |
| 0.75% $Eu^{3+}$ | 10.70 |
| 1% $Eu^{3+}$ | 6.11 |
| 2% $Eu^{3+}$ | 5.31 |
| 4% $Eu^{3+}$ | 4.43 |
| 8% $Eu^{3+}$ | 3.13 |

### 3.4 $Pr^{3+}$ doped $NaAlGeO_4$: XRD, photoluminescence spectra, CIE 1931 diagram

The X-ray diffraction patterns of $NaAlGeO_4$ samples doped with different concentrations of $Pr^{3+}$ ions (0.1%, 0.25%, 0.5%, 0.75%, 1%, 2%, and 4%) confirm the formation of a single-phase crystalline structure (**Figure 21**). All diffraction peaks are well indexed to the standard $NaAlGeO_4$ phase, indicating that the incorporation of $Pr^{3+}$ ions does not introduce secondary phases or structural distortions beyond detection limits. The absence of impurity phases suggests that $Pr^{3+}$ ions successfully substitute into the host lattice without significantly altering its crystalline framework.

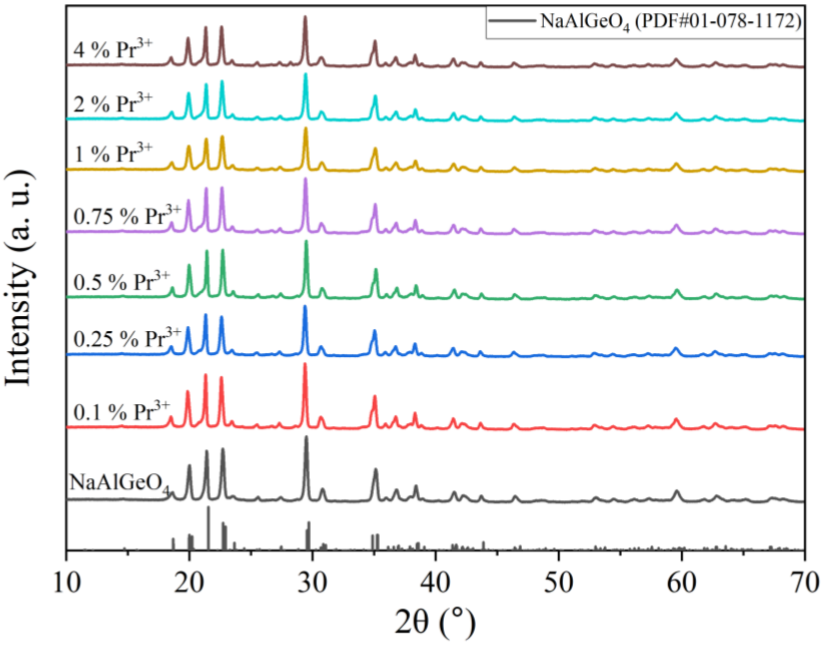

**Figure 21.** XRD patterns of $NaAlGeO_4$ samples doped with different concentrations of $Pr^{3+}$ ions. Black bars represent standard diffraction peaks of $NaAlGeO_4$.

The photoluminescence excitation and emission spectra of $NaAlGeO_4:Pr^{3+}$ are displayed in **Figure 22**. The excitation spectrum ($\lambda_{em}$ = 645 nm) exhibits characteristic absorption bands assigned to the transitions from the $Pr^{3+}$ ground state ($^3H_4$) to higher energy states. The most prominent excitation bands are observed in the 400-500 nm region, corresponding to $^3H_4 \rightarrow {}^3P_2$ and $^3H_4 \rightarrow {}^3P_0$ transitions. The broad absorption band observed within the 250–350 nm range can be attributed to the 4f → 5d transitions of $Pr^{3+}$. In rare-earth doped materials, these transitions typically occur in the UV range (200–350 nm), depending on the host matrix. Unlike the sharp 4f-4f transitions, the 5d levels are more sensitive to the surrounding crystal field, resulting in significant splitting and broadening of the absorption band.

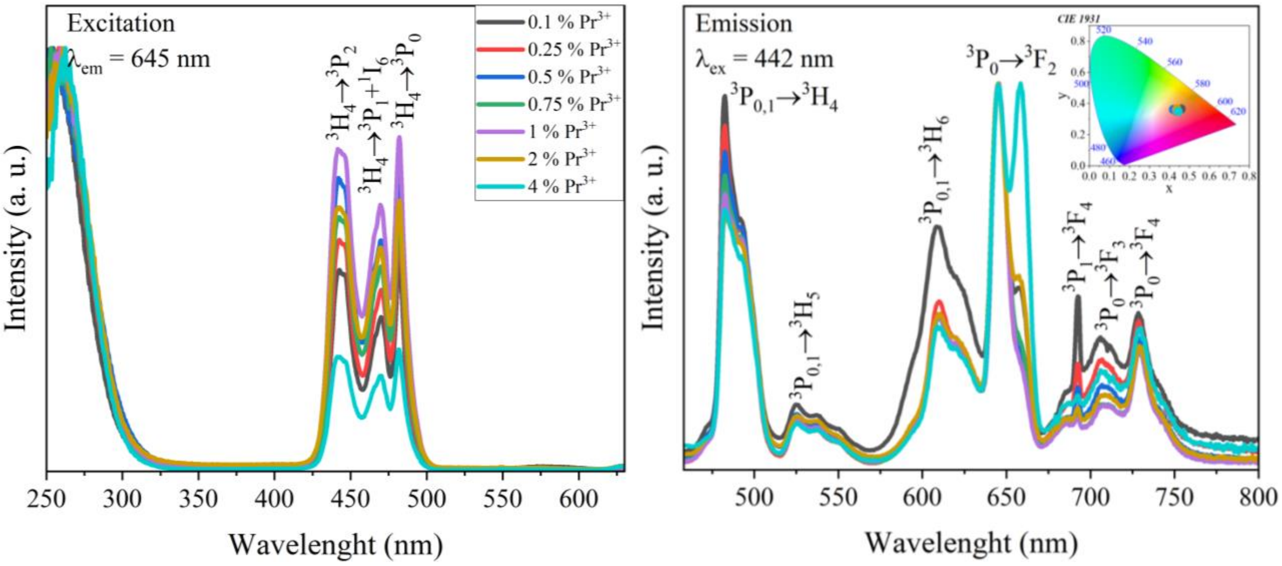

**Figure 22.** Photoluminescence excitation ($\lambda_{em}$ = 645 nm) and emission ($\lambda_{ex}$ = 442 nm) spectra of $NaAlGeO_4$:Pr samples. Inset shows CIE 1931 chromaticity diagram.

The emission spectrum ($\lambda_{ex}$ = 442 nm) presents intense peaks in the visible and near-infrared regions, corresponding to the transitions from the excited $^3P_0$ state to lower energy levels ($^3P_0 \rightarrow {}^3H_4$, $^3P_0 \rightarrow {}^3H_5$, and $^3P_0 \rightarrow {}^3F_2$, among others). The 0.1% $Pr^{3+}$-doped sample showed the highest emission intensity, with a pronounced red emission around 612 nm – an especially attractive feature for red phosphor applications. This behaviour aligns well with the findings of Tao Zhang et al., who reported that $LiYGeO_4$ doped with 0.15% $Pr^{3+}$ exhibits intense red long-persistent luminescence, lasting over 1500 seconds after 10 minutes of pre-irradiation with a 254 nm UV lamp. Red emission was primarily attributed to three transitions: $^1D_2 \rightarrow {}^3H_4$ (601 nm), $^3P_0 \rightarrow {}^3H_6$ (612 nm), and $^3P_0 \rightarrow {}^3F_2$ (651 nm) [18]. The inset in **Figure 22** shows the CIE 1931 chromaticity diagram, confirming the red colour emission of $NaAlGeO_4:Pr^{3+}$.

### 3.5 $Sm^{3+}$ doped $NaAlGeO_4$: XRD, photoluminescence spectra, CIE 1931 diagram, decay lifetimes, QY

To verify the phase purity, XRD was performed on $NaAlGeO_4:Sm^{3+}$ samples with doping concentrations ranging from 0.1% to 4%, as shown in **Figure 23**. The XRD patterns of $NaAlGeO_4:Sm^{3+}$ samples reveal that at lower doping concentrations (0.1%–1%), the material maintains a pure crystalline phase with no detectable impurity peaks, indicating that $Sm^{3+}$ ions successfully integrate into the host lattice without disrupting its structural integrity. However, at higher $Sm^{3+}$ concentrations of 2% and 4%, unidentified additional peaks appear in the XRD patterns, suggesting the formation of secondary phases.

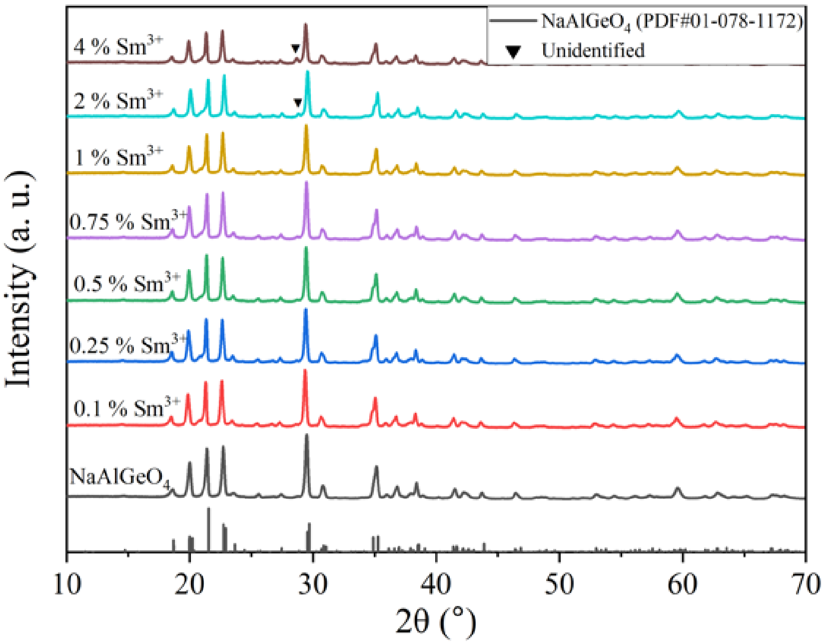

**Figure 23.** XRD patterns of $NaAlGeO_4$ samples doped with different concentrations of $Sm^{3+}$ ions. Black bars represent standard diffraction peaks of $NaAlGeO_4$.

The photoluminescence spectra of $NaAlGeO_4:Sm^{3+}$ are presented in **Figure 24**. The excitation spectrum ($\lambda_{em}$ = 600 nm) exhibits multiple absorption bands associated with the $Sm^{3+}$ transitions from the $^{6}H_{5/2}$ ground state to excited states such as $^{6}P_{3/2}$, $^{6}P_{7/2}$, and $^{4}K_{11/2}$. The strongest absorption is observed at ~400 nm, corresponding to the $^{6}H_{5/2} \rightarrow {}^{6}P_{3/2}$ transition. As the doping concentration increases, the excitation intensity decreases, with the 0.25% sample exhibiting the highest intensity.

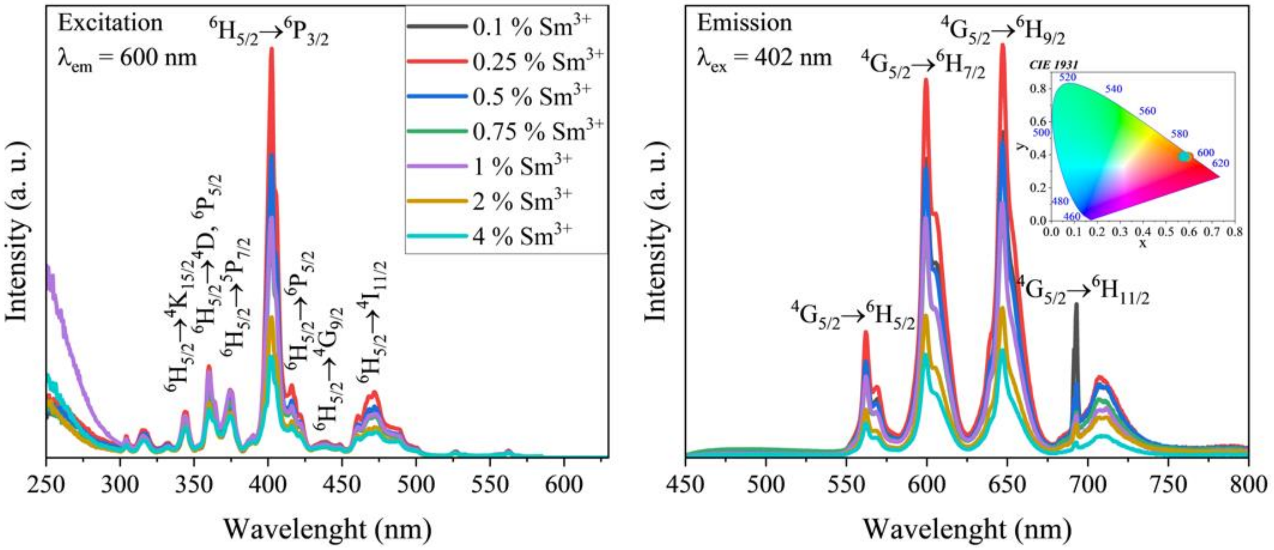

**Figure 24.** Photoluminescence excitation ($\lambda_{em}$ = 600 nm) and emission ($\lambda_{ex}$ = 402 nm) spectra of $NaAlGeO_4$:Sm samples. Inset shows CIE 1931 chromaticity diagram.

The emission spectrum ($\lambda_{ex}$ = 402 nm) displays sharp peaks corresponding to characteristic $Sm^{3+}$ transitions. The dominant emission at 650 nm originates from the $^{4}G_{5/2} \rightarrow {}^{6}H_{9/2}$ transition, followed by additional emissions in the orange-red region, including $^{4}G5/2 \rightarrow {}^{6}H_{5/2}$ and $^{4}G_{5/2} \rightarrow {}^{6}H_{7/2}$. Jie Zhang et al. reported that $NaYGeO_4$ doped with $Sm^{3+}$ exhibits a dominant emission peak at

650 nm, corresponding to the electric dipole transition $^4G_{5/2} \rightarrow {}^6H_{9/2}$. This suggests that $Sm^{3+}$ ions occupy lattice sites without inversion symmetry within the $NaYGeO_4$ host structure [22]. The chromaticity diagram (inset in **Figure 24**) confirms the orange-red emission of $NaAlGeO_4$: $Sm^{3+}$, with all samples clustering closely.

The luminescence decay times of $NaAlGeO_4$:$Sm^{3+}$ samples with varying $Sm^{3+}$ concentrations (0.1%–4%) are shown in **Table 7** and **Figure 25**. At a low doping concentration of 0.1%, the sample exhibited the longest average decay time of 1896.76 µs. As the doping concentration increased, the average decay time decreased, reaching 1542.79 µs at 0.25% and 1089.75 µs at 0.5%. The decay time then slightly increased at 0.75% (1146.56 µs) and 1% (1212.48 µs), before stabilising around 1377.65 µs at 2% and 1355.18 µs at 4%. This suggests that, while the decay time decreases with increasing doping, higher concentrations may lead to some stabilisation in the decay rate, indicating a balance between radiative and non-radiative processes.

**Table 7.** Decay kinetics data of $Na_{1-x}AlGe_{1-0.5x}O_4$:$Sm_x$ samples.

| Sample | $\tau_1$, µs | Rel, % | $\tau_2$, µs | Rel, % | $\tau_{avg}$, µs |
|---|---|---|---|---|---|
| 0.1% | 681.35 | 24.43 | 2289.67 | 75.57 | 1896.76 |
| 0.25% | 546.56 | 30.18 | 1973.42 | 69.82 | 1542.79 |
| 0.5% | 349.98 | 38.88 | 1560.33 | 61.12 | 1089.75 |
| 0.75% | 328.97 | 41.46 | 1725.61 | 58.54 | 1146.56 |
| 1% | 331.27 | 38.17 | 1756.48 | 61.83 | 1212.48 |
| 2% | 304.79 | 34.56 | 1944.25 | 65.44 | 1377.65 |
| 4% | 352.99 | 33.89 | 1868.94 | 66.11 | 1355.18 |

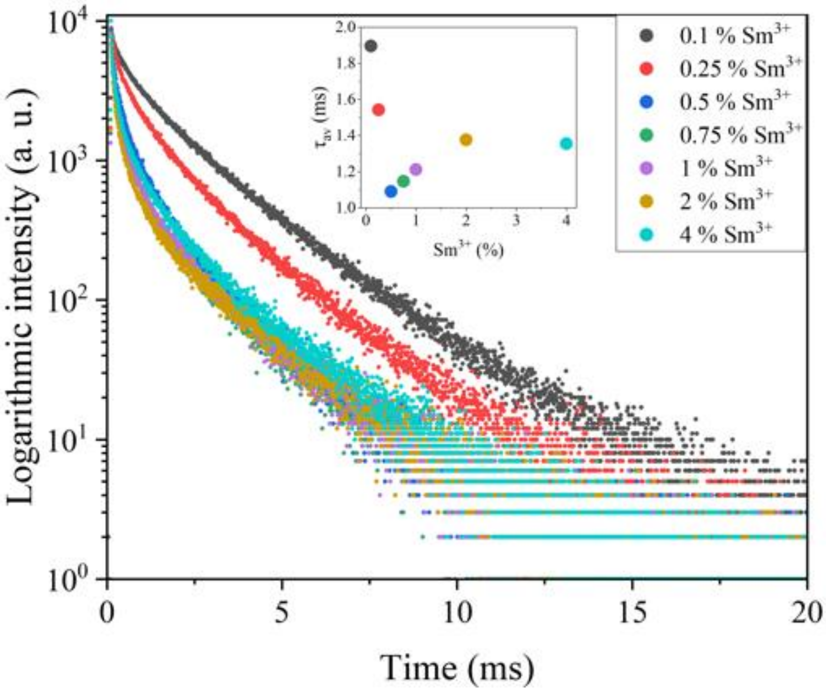

**Figure 25.** Luminescence emission decay times of $NaAlGeO_4$ samples with varying $Sm^{3+}$ concentrations.

The quantum yield of Sm-doped $NaAlGeO_4$ samples exhibits a strong dependence on dopant concentration, revealing an optimal emission efficiency at lower $Sm^{3+}$ levels (**Table 8**). The highest QY of 3.61% is observed for the 0.25% $Sm^{3+}$-doped sample, followed closely by the 0.1% $Sm^{3+}$ sample at 3.41%. A sharp decline in QY is noted with increasing dopant concentration beyond 0.25%, dropping to 1.03% at 0.5% $Sm^{3+}$ and further decreasing to 0.02% for 4% $Sm^{3+}$. This trend suggests concentration quenching, likely due to enhanced non-radiative energy transfer at higher $Sm^{3+}$ loadings, which reduces the overall luminescence efficiency.

**Table 8.** Quantum yields of doped $Na_{1-x}AlGe_{1-0.5x}O_4$ samples, where x is $Sm^{3+}$.

| Sample | Quantum yield, % |
|---|---|
| 0.1% $Sm^{3+}$ | 3.41 |
| 0.25% $Sm^{3+}$ | 3.61 |
| 0.5% $Sm^{3+}$ | 1.03 |
| 0.75% $Sm^{3+}$ | 1.07 |
| 1% $Sm^{3+}$ | 0.49 |
| 2% $Sm^{3+}$ | 0.38 |
| 4% $Sm^{3+}$ | 0.02 |

### 3.6 $Tb^{3+}$ doped $NaAlGeO_4$: XRD, photoluminescence spectra, CIE 1931 diagram, decay lifetimes

The crystallographic phase purity and structural integrity of $NaAlGeO_4:Tb^{3+}$ phosphors were examined using X-ray diffraction analysis (**Figure 26**). The diffraction patterns for all $Tb^{3+}$-doped samples closely match the standard $NaAlGeO_4$ phase (PDF#01–078–1172), indicating that the host lattice remains intact upon $Tb^{3+}$ incorporation. As the $Tb^{3+}$ concentration increases, no significant shifts in peak positions are observed, suggesting that the dopant ions substitute into the lattice without substantial distortion. However, at higher doping levels (≥2% $Tb^{3+}$), the appearance of additional peaks (marked by black triangles) suggests the formation of secondary phases. These unidentified peaks indicate potential solubility limits for $Tb^{3+}$ in the $NaAlGeO_4$ matrix.

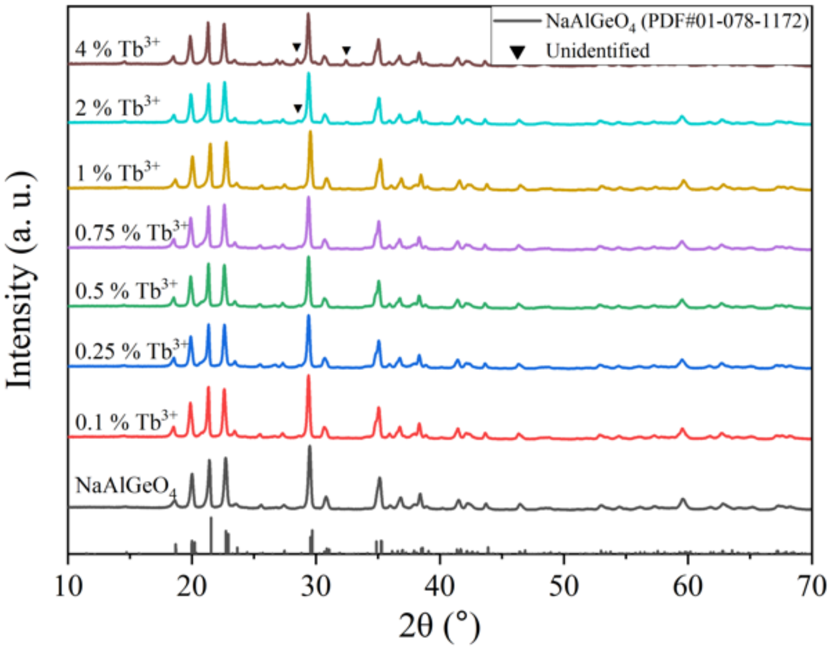

**Figure 26.** XRD patterns of NaAlGeO$_4$ samples doped with different concentrations of Tb$^{3+}$ ions. Black bars represent standard diffraction peaks of NaAlGeO$_4$.

The photoluminescence properties of NaAlGeO$_4$:Tb$^{3+}$ phosphors were investigated through excitation and emission spectroscopy (**Figure 27**). The excitation spectra ($\lambda_{em}$ = 549 nm) exhibit characteristic Tb$^{3+}$ transitions, including the broad 4f → 5d absorption band below 350 nm and f-f transitions such as $^7F_6 \rightarrow {}^5D_4$ about 500 nm. The emission spectra ($\lambda_{ex}$ = 377 nm) reveal strong luminescence peaks corresponding to Tb$^{3+}$ transitions, notably the dominant $^5D_4 \rightarrow {}^7F_5$ transition at 549 nm, alongside weaker emissions from $^5D_4 \rightarrow {}^7F_6$, $^5D_4 \rightarrow {}^7F_4$, and $^5D_4 \rightarrow {}^7F_3$. The intensity of these emissions increases with Tb$^{3+}$ concentration up to an optimal doping level – 1% sample. These results are consistent with previous studies, which reported the strongest green emission peak for NaYGeO$_4$:Tb$^{3+}$ at 554 nm [63], 552 nm [23], and 542 nm [20], and for LiYGeO$_4$:Tb$^{3+}$ at 549 nm [16] and 550 nm [12,14,15,17]. The inset of the emission spectra presents the CIE 1931 chromaticity diagram, confirming the green emission characteristics of the phosphors.

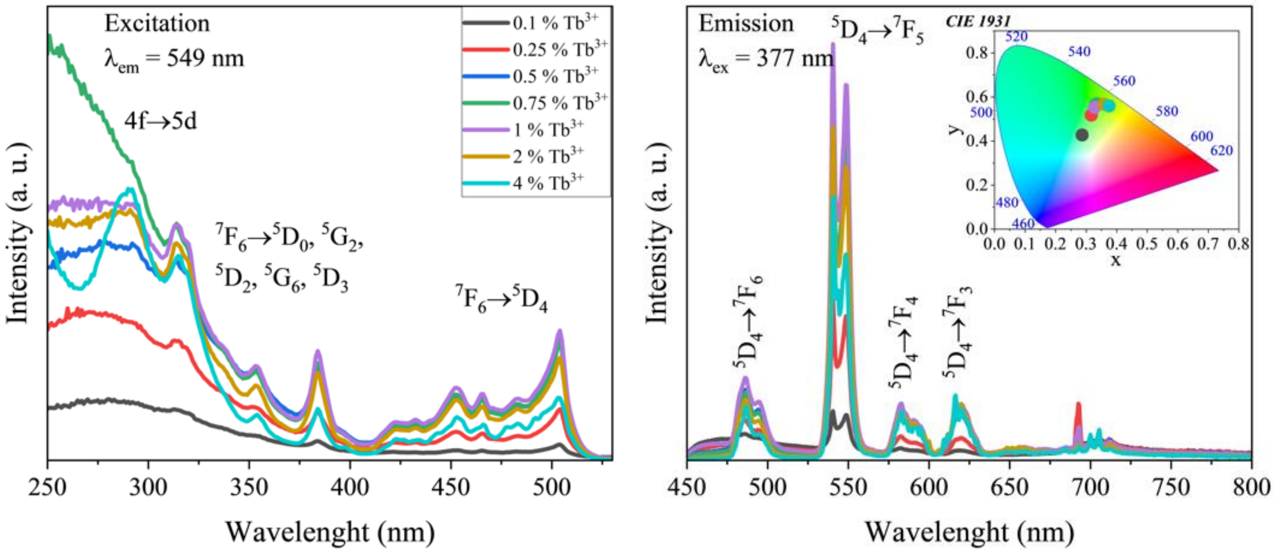

**Figure 27.** Photoluminescence excitation ($\lambda_{em}$ = 549 nm) and emission ($\lambda_{ex}$ = 377 nm) spectra of NaAlGeO$_4$:Tb samples. Inset shows CIE 1931 chromaticity diagram.

The luminescence decay dynamics of $NaAlGeO_4:Tb^{3+}$ phosphors were investigated to assess the impact of $Tb^{3+}$ concentration on emission lifetime (**Table 9** and **Figure 28**). The decay profiles reveal a concentration dependent trend, where the 0.1% $Tb^{3+}$-doped sample exhibits the longest decay time – 2342 μs. As the $Tb^{3+}$ concentration increases, the decay times progressively shorten, with the 4% $Tb^{3+}$ sample displaying the most rapid luminescence quenching – 1624 μs. This trend suggests concentration quenching effects, likely due to non-radiative relaxation pathways at higher doping levels. These results emphasize the need for an optimal doping level to balance emission intensity and lifetime, maximizing phosphor efficiency for potential applications in optoelectronic devices.

**Table 9.** Decay kinetics data of $Na_{1-x}AlGe_{1-0.5x}O_4:Tb_x$ samples.

| Sample | $\tau_1$, μs | Rel, % | $\tau_2$, μs | Rel, % | $\tau_{avg}$, μs |
|---|---|---|---|---|---|
| 0.1% | 1925.81 | 73.55 | 3500.23 | 26.45 | 2342.24 |
| 0.25% | 1334.02 | 29.91 | 2536.21 | 70.09 | 2176.63 |
| 0.5% | 1383.32 | 32.00 | 2595.61 | 68.00 | 2207.68 |
| 0.75% | 1067.13 | 21.87 | 2353.69 | 78.13 | 2072.32 |
| 1% | 619.18 | 9.74 | 2214.11 | 90.26 | 2058.76 |
| 2% | 279.30 | 5.44 | 2111.29 | 94.56 | 2011.63 |
| 4% | 147.14 | 23.71 | 2083.12 | 76.29 | 1624.10 |

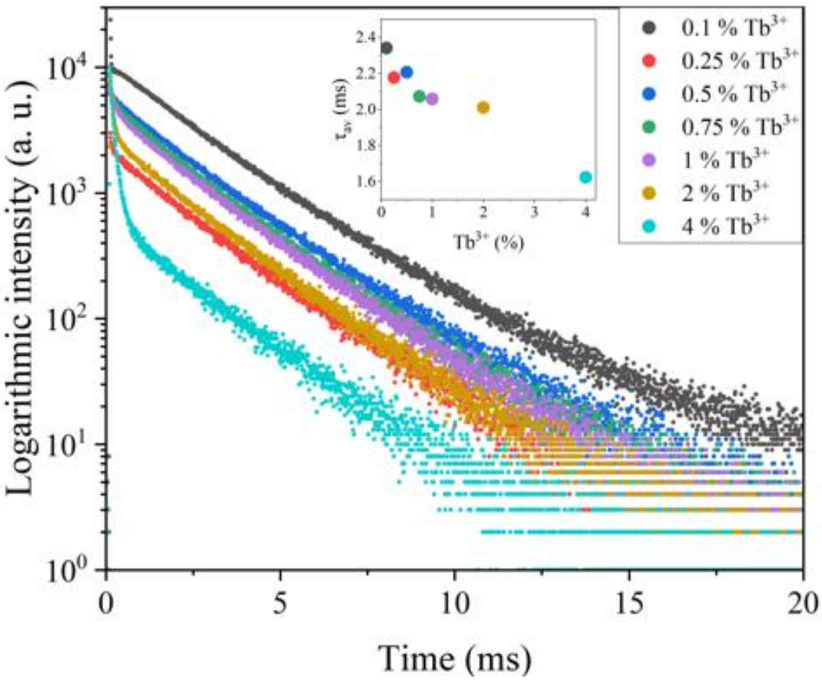

**Figure 28.** Luminescence emission decay times of $NaAlGeO_4$ samples with varying $Tb^{3+}$ concentrations.

# CONCLUSIONS

1. $NaAlGeO_4$ phosphors doped with $Bi^{3+}$, $Dy^{3+}$, $Eu^{3+}$, $Pr^{3+}$, $Sm^{3+}$, and $Tb^{3+}$ ions were successfully synthesised using the high-temperature solid-state method. X-ray diffraction analysis confirmed that the main $NaAlGeO_4$ structure remained stable across all samples. However, at higher doping levels (2–8%), an increase in unidentified diffraction peaks indicated the onset of phase segregation or secondary phase formation.
2. Each dopant exhibited distinct photoluminescence behaviour. $Bi^{3+}$-doped samples showed a strong blue emission at 420 nm, with maximum intensity achieved at 0.2% doping. $Dy^{3+}$-doped samples emitted yellow light at 574 nm under 386 nm excitation, with peak intensity observed at 0.1% doping. $Eu^{3+}$-doped samples displayed characteristic red emission at 611 nm under 393 nm excitation, with a decline in intensity noted at concentrations above 0.75%. $Pr^{3+}$-doped phosphors exhibited visible and near-infrared emissions, with a prominent red peak at 612 nm at 0.1% doping. $Sm^{3+}$-doped samples showed dominant orange-red emission around 600 nm, with maximum intensity at 0.25% doping. $Tb^{3+}$-doped samples demonstrated strong green emission at 549 nm, with the highest intensity recorded at 1% doping.
3. The average decay times decreased with increasing dopant concentration for most dopants. $Bi^{3+}$ and $Dy^{3+}$ samples exhibited longer decay times at 0.1% doping, with $Dy^{3+}$ reaching 538.19 μs. $Eu^{3+}$-doped samples showed the longest decay (1589.42 μs) at 0.25% doping before sharply declining. $Sm^{3+}$-doped samples achieved the longest average decay time (1896.76 μs) at 0.1% doping, while $Tb^{3+}$-doped samples recorded the highest decay time (2342 μs) at 0.1% doping.
4. Quantum efficiency measurements identified optimal doping concentrations for each dopant. The highest quantum yields were obtained at low concentrations: 5.80% for 0.2% $Bi^{3+}$, 3.94% for 0.5% $Dy^{3+}$, 14.27% for 0.5% $Eu^{3+}$, and 3.61% for 0.25% $Sm^{3+}$. Beyond these optimal doping levels, a significant decrease in quantum yield was observed, attributed to concentration quenching effects.

# BIBLIOGRAPHY

[1] J.H. Kim, K.H. Yoon, Fabrication and Performance of ACTFEL Display Devices Using Manganese-Doped Zinc Germanate as a Green-Emitting Electroluminescent Layer, Journal of the Korean Physical Society 56 (2010) 1861–1865. https://doi.org/10.3938/jkps.56.1861.

[2] R.M. Gunji, E.V. de A. Santos, C.D.S. Bordon, J.A.M. Garcia, L.A. Gómez-Malagón, L.R.P. Kassab, Germanate glass layer containing Eu3+ ions and gold nanoparticles for enhanced silicon solar cell performance, J Lumin 226 (2020) 117497. https://doi.org/10.1016/j.jlumin.2020.117497.

[3] D. Gao, F. Gao, Q. Kuang, X. Zhang, Z. Zhang, Y. Pan, R. Chai, H. Jiao, Zinc Germanate Nanophosphors with Persistent Luminescence for Multi-Mode Imaging of Latent Fingerprints, ACS Appl Nano Mater 5 (2022) 9929–9939. https://doi.org/10.1021/acsanm.2c02163.

[4] M.J. Oviedo, O.E. Contreras, Y. Rosenstein, R. Vazquez-Duhalt, Z.S. Macedo, G.G. Carbajal-Arizaga, G.A. Hirata, New Bismuth Germanate Oxide Nanoparticle Material for Biolabel Applications in Medicine, J Nanomater 2016 (2016) 1–10. https://doi.org/10.1155/2016/9782625.

[5] A.S. Gouveia-Neto, W.S. Souza, R.O. Domingues, E.B. da Costa, L.A. Bueno, Color tunable green-yellow-orange-red erbium/europium codoped fluorolead germanate glass phosphor for application in LED illumination technology, in: K.P. Streubel, H. Jeon, L.-W. Tu, M. Strassburg (Eds.), 2013: p. 86411E. https://doi.org/10.1117/12.2001118.

[6] Q. Zhang, X. Wang, Y. Wang, A novel germanate based red-emitting phosphor with high efficiency, high color purity and thermal stability for white light-emitting diodes and field emission displays, Inorg Chem Front 7 (2020) 1034–1045. https://doi.org/10.1039/C9QI01428D.

[7] J. Shi, X. Sun, S. Zheng, X. Fu, Y. Yang, J. Wang, H. Zhang, Super-Long Persistent Luminescence in the Ultraviolet A Region from a Bi3+-Doped LiYGeO4 Phosphor, Adv Opt Mater 7 (2019) 1900526. https://doi.org/10.1002/adom.201900526.

[8] T. Dai, G. Ju, Y. Lv, Y. Jin, H. Wu, Y. Hu, Luminescence properties of novel dual-emission (UV/red) long afterglow phosphor LiYGeO4: Eu3+, J Lumin 237 (2021) 118193. https://doi.org/10.1016/J.JLUMIN.2021.118193.

[9] Z. Wang, Z. Fu, T. Sheng, J. Li, Enhanced temperature sensing properties in LiYGeO4: Eu3+ phosphors via Bi3+ doping, J Lumin 270 (2024) 120554. https://doi.org/10.1016/j.jlumin.2024.120554.

[10] P. Shao, P. Xiong, Y. Xiao, Q. Chen, Y. Sun, N. Yan, D. Chen, Z. Yang, Novel spectral band: ultraviolet A mechanoluminescence from Bi3+-doped LiYGeO4, J Mater Chem C Mater 10 (2022) 16670–16678. https://doi.org/10.1039/D2TC03585E.

[11] S. Zhou, B. Lou, C.-G. Ma, M. Yin, First-principles study on persistent luminescence mechanism of LiYGeO4:Eu3+, Journal of Rare Earths (2022). https://doi.org/10.1016/j.jre.2022.07.016.

[12] X. Zhang, H. Song, R. Cui, K. Guo, M. Zhang, C. Deng, Luminescence properties of multicolor-tunable emitting LiYGeO4: Tb3+, Eu3+ phosphors with excellent thermal stability for WLEDs, Mater Res Bull 167 (2023) 112401. https://doi.org/10.1016/j.materresbull.2023.112401.

[13] M. Misevicius, E. Griniuk, R. Ramanauskas, Solid-state synthesis of LiYGeO4 and luminescence properties of Dy-doped samples, Mater Chem Phys 306 (2023) 128082. https://doi.org/10.1016/j.matchemphys.2023.128082.

[14] H. Wang, X. Wang, S. Liu, T. Mei, Y. Fan, L. Kang, F. Xin, M. Xing, Y. Fu, X. Luo, Y. Tian, Color-tunable photoluminescence and persistent luminescence in a single LiYGeO4:Tb3+ phosphor, Mater Res Express 9 (2022) 076201. https://doi.org/10.1088/2053-1591/ac82a7.

[15] G. Ou, H. Song, X. Gong, R. Cui, C. Deng, Synthesis and photoluminescence properties of a novel green-emitting LiYGeO4 :Tb3+ long afterglow phosphor, Luminescence 37 (2022) 2018–2027. https://doi.org/10.1002/bio.4386.

[16] P. Shao, P. Xiong, D. Jiang, Z. Chen, Y. Xiao, Y. Sun, D. Chen, Z. Yang, Tunable and enhanced mechanoluminescence in LiYGeO4:Tb3+ via Bi3+ → Tb3+ energy transfer, J Mater Chem C Mater 11 (2023) 2120–2128. https://doi.org/10.1039/D2TC04902C.

[17] Y. Lv, N. Zhao, C. Li, C. Lin, S. You, Improved synthetic method for the color-tunable LiYGeO4:Tb3+ persistent phosphor toward information storage, Ceram Int 50 (2024) 51484–51490. https://doi.org/10.1016/j.ceramint.2024.10.066.

[18] T. Zhang, H. Guo, Q. Shi, J. Qiao, C. Cui, P. Huang, L. Wang, Investigation of a novel Pr3+-activated LiYGeO4 phosphor with red long-persistent luminescence, J Lumin 267 (2024) 120382. https://doi.org/10.1016/j.jlumin.2023.120382.

[19] X. Yin, H. Zhong, L. Liu, J. Shi, X. Sun, Y. Zhang, X-ray-activated Bi3+/Pr3+ co-doped LiYGeO4 phosphor with UV and NIR dual-emissive persistent luminescence, Journal of Rare Earths 42 (2024) 955–961. https://doi.org/10.1016/J.JRE.2023.03.008.

[20] E. Wang, K. Feng, J. Li, X. Zhou, X. Sun, Luminescence characteristics of NaYGeO4:Bi3+/Tb3+/Eu3+ phosphors, J Lumin 250 (2022) 119108. https://doi.org/10.1016/J.JLUMIN.2022.119108.

[21] B. Han, Y. Chen, B. Liu, J. Zhang, Solid state synthesis and luminescence properties of Eu3+ doped NaYGeO4 phosphors, Optik (Stuttg) 242 (2021) 167177. https://doi.org/10.1016/J.IJLEO.2021.167177.

[22] J. Zhang, B. Liu, Y. Dai, B. Han, Synthesis and luminescence properties of novel host-sensitized germanate phosphors NaYGeO4:Ln (Ln = Eu3+, Sm3+, Dy3+), Optik (Stuttg) 203 (2020) 163944. https://doi.org/10.1016/J.IJLEO.2019.163944.

[23] W. Zhao, X. Feng, B. Fan, Novel color tunable phosphors NaYGeO4: Tm3+, Tb3+, Eu3+ for ultraviolet excited white LEDs with good thermal stability, Journal of Materials Science: Materials in Electronics 31 (2020) 14434–14442. https://doi.org/10.1007/s10854-020-04003-4.

[24] B. Fan, W. Zhou, S. Qi, W. Zhao, Eu3+-doped NaYGeO4: A novel red-emitting phosphors for ultraviolet or blue chips excited white LEDs, J Solid State Chem 283 (2020) 121158. https://doi.org/10.1016/J.JSSC.2019.121158.

[25] A. Harnik, M. Misevičius, Solid-state synthesis and luminescence study of Bi or Eu-doped LiAlGeO4, Chemija 33 (2022). https://doi.org/10.6001/chemija.v33i4.4805.

[26] K.A. Soubbotin, V.A. Smirnov, S.V. Kovaliov, H.J. Scheel, E.V. Zharikov, Growth and spectroscopic investigation of new promising laser crystal chromium (IV) doped germanoeucryptite Cr4+:LiAlGeO4, Opt Mater (Amst) 13 (2000) 405–410. https://doi.org/10.1016/S0925-3467(99)00079-8.

[27] Z. Zhou, P. Xiong, H. Liu, M. Peng, Ultraviolet-A Persistent Luminescence of a Bi3+ -Activated LiScGeO4 Material, Inorg Chem 59 (2020) 12920–12927. https://doi.org/10.1021/acs.inorgchem.0c02007.

[28] Y. Zhang, D. Chen, W. Wang, S. Yan, J. Liu, Y. Liang, Long-lasting ultraviolet-A persistent luminescence and photostimulated persistent luminescence in Bi3+ -doped LiScGeO4 phosphor, Inorg Chem Front 7 (2020) 3063–3071. https://doi.org/10.1039/D0QI00578A.

[29] Z. Ye, Z. Wang, Q. Wu, X. Huo, H. Yang, Y. Wang, D. Wang, J. Zhao, H. Suo, P. Li, A single luminescence center ultra-broadband near-infrared LiScGeO4:Cr phosphor for biological tissue penetration, Dalton Transactions 50 (2021) 10092–10101. https://doi.org/10.1039/D1DT01244D.

[30] M. Sharonov, V. Petricevic, A. Bykov, R.R. Alfano, Near-infrared laser operation of Cr3+ centers in chromium-doped LiInGeO4 and LiScGeO4 crystals, Opt Lett 30 (2005) 851. https://doi.org/10.1364/OL.30.000851.

[31] S. Miao, Y. Liang, Y. Zhang, D. Chen, X.-J. Wang, Broadband Short-Wave Infrared Light-Emitting Diodes Based on Cr3+ -Doped LiScGeO4 Phosphor, ACS Appl Mater Interfaces 13 (2021) 36011–36019. https://doi.org/10.1021/acsami.1c10490.

[32] P.A. Sandomirskii, S.S. Meshalkin, I. V. Rozhdestvenskaya, L.N. Dem'yanets, T.G. Uvarova, Crystal structures of the D-phase of KAlGeO4 and the C-phase of NaAlGeO4, Sov. Phys. Crystallogr 31 (1986) 522–527.

[33] J. Barbier, M.E. Fleet, Investigation of phase relations in the (Na,K)AlGeO4 system, Phys Chem Miner 16 (1988). https://doi.org/10.1007/BF00220695.

[34] W. Sun, R. Pang, H. Li, D. Li, L. Jiang, S. Zhang, J. Fu, C. Li, Investigation of a novel color tunable long afterglow phosphor KGaGeO4:Bi3+ : luminescence properties and mechanism, J Mater Chem C Mater 5 (2017) 1346–1355. https://doi.org/10.1039/C6TC04012H.

[35] J. Shi, X. Sun, S. Zheng, X. Fu, Y. Yang, J. Wang, H. Zhang, Super-Long Persistent Luminescence in the Ultraviolet A Region from a Bi3+-Doped LiYGeO4 Phosphor, Adv Opt Mater 7 (2019). https://doi.org/10.1002/ADOM.201900526.

[36] L. V. Ermakova, I.I. Leonidov, Towards a new group of olivine-type afterglow phosphors: the case of Ca2GeO4:Dy3+, Mater Lett 233 (2018) 39–41. https://doi.org/10.1016/j.matlet.2018.08.125.

[37] N. Bednarska-Adam, J. Pisarska, M. Kuwik, T. Goryczka, M. Zubko, W.A. Pisarski, Synthesis and photoluminescent characterization of ceramic phosphors Li2MgGeO4 :Ln3+ (Ln3+ = Pr3+ or Tm3+) under different excitation wavelengths, RSC Adv 13 (2023) 12386–12393. https://doi.org/10.1039/D3RA00500C.

[38] H.-M. Yang, Z. Wang, M.-L. Gong, H. Liang, Luminescence properties of a novel red emitting phosphor, Mg2GeO4:Sm3+, J Alloys Compd 488 (2009) 331–333. https://doi.org/10.1016/j.jallcom.2009.08.123.

[39] K.V.R. Murthy, H.S. Virk, Luminescence Phenomena: An Introduction, Defect and Diffusion Forum 347 (2013) 1–34. https://doi.org/10.4028/www.scientific.net/DDF.347.1.

[40] K.V.R. Murthy, H.S. Virk, Luminescence Phenomena: An Introduction, Defect and Diffusion Forum 347 (2013) 1–34. https://doi.org/10.4028/www.scientific.net/DDF.347.1.

[41] I.T. Sorokina, Crystalline Mid-Infrared Lasers, in: Solid-State Mid-Infrared Laser Sources, Springer Berlin Heidelberg, Berlin, Heidelberg, n.d.: pp. 262–358. https://doi.org/10.1007/3-540-36491-9_7.

[42] J.F. Liu, Luminescence properties of bismuth-doped SrO-B2O3 glasses with multiple valences state, Optik (Stuttg) 126 (2015) 4115–4118. https://doi.org/10.1016/j.ijleo.2015.07.207.

[43] Y. Zorenko, V. Gorbenko, T. Zorenko, P. Malinowski, V. Jary, R. Kucerkova, A. Beitlerova, J.A. Mares, M. Nikl, A. Fedorov, Luminescent and scintillation properties of Bi3+ doped Y2SiO5 and Lu2SiO5 single crystalline films, J Lumin 154 (2014) 525–530. https://doi.org/10.1016/J.JLUMIN.2014.05.030.

[44] Q. Dong, C. Huang, X. Huang, L. He, Multicolor luminescence from CaZnOS: Bi3+, Eu3+ for stress sensing and multimode anti-counterfeiting, J Alloys Compd 967 (2023) 171687. https://doi.org/10.1016/J.JALLCOM.2023.171687.

[45] O. Bagi Aljewaw, M.K.A. Karim, H. Mohamed Kamari, M.H. Mohd Zaid, N. Mohd Noor, I.N. Che Isa, M.H. Abu Mhareb, Impact of Dy2O3 Substitution on the Physical, Structural and Optical Properties of Lithium–Aluminium–Borate Glass System, Applied Sciences 10 (2020) 8183. https://doi.org/10.3390/app10228183.

[46] I. Kashif, A. Ratep, Judd-Ofelt and luminescence study of Dysprosium-doped lithium borosilicate glasses for lasers and w-LEDs, Boletin de La Sociedad Espanola de Ceramica y Vidrio 61 (2022) 622–633. https://doi.org/10.1016/J.BSECV.2021.06.001.

[47] N.A. Razak, S. Hashim, M.H.A. Mhareb, Y.S.M. Alajerami, S.A. Azizan, N. Tamchek, Impact of Eu3+ Ions on Physical and Optical Properties of Li2 O-Na2O-B2O3 Glass, Chinese Journal of Chemical Physics 29 (2016) 395–400. https://doi.org/10.1063/1674-0068/29/cjcp1511226.

[48] J. Kappelhoff, B. Greve, T. Jüstel, On the temperature dependent photoluminescence of nanoscale LuPO4:Eu3+ and their application for bioimaging, RSC Adv 14 (2024) 29992–29998. https://doi.org/10.1039/D4RA01190B.

[49] Z. Liu, R. Wang, D. Chen, Dual-mode optical temperature sensing properties of PIN-PMN-PT:Pr3+ ceramic based on fluorescence intensity ratios and lifetimes, Journal of Materials Science: Materials in Electronics 33 (2022) 3748–3756. https://doi.org/10.1007/s10854-021-07566-y.

[50] H. Tanaka, S. Kalusniak, M. Badtke, M. Demesh, N. V. Kuleshov, F. Kannari, C. Kränkel, Visible solid-state lasers based on Pr3+ and Tb3+, Prog Quantum Electron 84 (2022) 100411. https://doi.org/10.1016/J.PQUANTELEC.2022.100411.

[51] A.K. Bedyal, V. Kumar, O.M. Ntwaeaborwa, H.C. Swart, A promising orange-red emitting nanocrystalline NaCaBO3:Sm3+ phosphor for solid state lightning, Mater Res Express 1 (2014) 015006. https://doi.org/10.1088/2053-1591/1/1/015006.

[52] I. Ullah, I. Khan, S.K. Shah, S.A. Khattak, M. Shoaib, J. Kaewkhao, T. Ahmad, E. Ahmed, G. Rooh, A. Khan, Luminescence properties of Sm3+ doped Na2B4O7 glasses for lighting application, J Lumin 230 (2021) 117700. https://doi.org/10.1016/J.JLUMIN.2020.117700.

[53] D. Bayoudhi, C. Bouzidi, E. Matei, M. Secu, A. Catalin Galca, Optical characterization of Sm3+ doped phosphate glasses for potential orange laser applications, J Lumin 265 (2024) 120204. https://doi.org/10.1016/J.JLUMIN.2023.120204.

[54] M. Shkir, A.S. Altowyan, F. Maiz, J. Hakami, Influence of incorporation of samarium (Sm3+) on the structural and optoelectronic properties of In2S3 thin film for photodetector applications, J Photochem Photobiol A Chem 441 (2023) 114736. https://doi.org/10.1016/J.JPHOTOCHEM.2023.114736.

[55] P. Biswas, V. Kumar, Kamni, The structural and spectral study of LiSrVO4:Tb3+ phosphor for UV-shifted imaging devices, Mater Today Proc 28 (2019) 1018–1023. https://doi.org/10.1016/J.MATPR.2019.12.342.

[56] I.P. Machado, V.C. Teixeira, C.C.S. Pedroso, H.F. Brito, L.C.V. Rodrigues, X-ray scintillator Gd2O2S:Tb3+ materials obtained by a rapid and cost-effective microwave-assisted solid-state synthesis, J Alloys Compd 777 (2019) 638–645. https://doi.org/10.1016/J.JALLCOM.2018.10.348.

[57] G. Blasse, A. Bril, Structure and Eu3+-fluorescence of lithium and sodium lanthanide silicates and germanates, Journal of Inorganic and Nuclear Chemistry 29 (1967) 2231–2241. https://doi.org/10.1016/0022-1902(67)80277-X.

[58] M.A. Melkozerova, T. V. Dyachkova, A.P. Tyutyunnik, A.N. Enyashin, A.Y. Chufarov, Y. V. Baklanova, V.G. Zubkov, Polymorphic transformations of NaYGeO4 olivine under high pressure and high temperature, Ceram Int 49 (2023) 6856–6863. https://doi.org/10.1016/J.CERAMINT.2022.10.173.

[59] R.F. Casten, C.W. Beausang, Gamma-Ray Spectroscopy, Encyclopedia of Physical Science and Technology (2003) 433–454. https://doi.org/10.1016/B0-12-227410-5/00273-8.

[60] E. Álvarez, Ma.E. Zayas, D. Rodríguez-Carvajal, F. Félix-Domínguez, R.P. Duarte-Zamorano, C. Falcony, U. Caldiño, Cold white light generation through the simultaneous emission from Ce3+ and Tb3+ in sodium germanate glass, Opt Mater (Amst) 37 (2014) 451–456. https://doi.org/10.1016/j.optmat.2014.06.038.

[61] Y. Zhong, T. Su, J. Xie, C. Wang, W. Wang, Y. Pan, X. Wei, Y. Li, Anti-thermal quenching and self-reduction characteristics in Mn2+-doped LiScGeO4: Dual temperature effects on unique emission peak shifts, Ceram Int 51 (2025) 9292–9300. https://doi.org/10.1016/J.CERAMINT.2024.12.364.

[62] K. Cheng, C. Li, H. Xiang, Y. Sun, L. Fang, LiYGeO4: Novel low-permittivity microwave dielectric ceramics with intrinsic low sintering temperature, Mater Lett 228 (2018) 96–99. https://doi.org/10.1016/J.MATLET.2018.05.124.

[63] J. Ma, Y. Li, W. Hu, W. Wang, J. Zhang, J. Yang, Y. Wang, A terbium activated multicolour photoluminescent phosphor for luminescent anticounterfeiting, Journal of Rare Earths 38 (2020) 1039–1043. https://doi.org/10.1016/j.jre.2019.09.008.

[64] R.D. Shannon, Revised effective ionic radii and systematic studies of interatomic distances in halides and chalcogenides, Acta Crystallographica Section A 32 (1976) 751–767. https://doi.org/10.1107/S0567739476001551.

[65] A. López de Guereñu, D.T. Klier, T. Haubitz, M.U. Kumke, Influence of Gd3+ doping concentration on the properties of Na(Y,Gd)F4:Yb3+, Tm3+ upconverting nanoparticles and their long-term aging behavior, Photochemical & Photobiological Sciences 21 (2022) 235–245. https://doi.org/10.1007/s43630-021-00161-4.

[66] D. Gao, Y. Li, L. Cheng, S. Liu, S. Xu, X. Li, J. Zhang, X. Zhang, Y. Cao, Y. Wang, X. Wang, Y. Zhang, X. Sha, L. Wang, B. Chen, Concentration effects of fluorescence quenching and optical transition properties of Dy3+ doped NaYF4 phosphor, J Alloys Compd 895 (2022) 162616. https://doi.org/10.1016/J.JALLCOM.2021.162616.

# SUMMARY

## VILNIUS UNIVERSITY
## FACULTY OF CHEMISTRY AND GEOSCIENCES

GABIJA JANUŠAUSKAITĖ

## Synthesis and Investigation of the Luminescent Properties of $NaAlGeO_4$ Doped with $Bi^{3+}$, $Dy^{3+}$, $Eu^{3+}$, $Pr^{3+}$, $Sm^{3+}$, and $Tb^{3+}$ Ions

Efficient and thermally stable phosphors are essential for solid-state lighting, bioimaging, and optical sensing applications. The aim of this study is to investigate the luminescence properties of $Na_{1–x}AlGe_{1–0.5x}GeO_4$-based phosphors doped with trivalent $Bi^{3+}$, $Dy^{3+}$, $Eu^{3+}$, $Pr^{3+}$, $Sm^{3+}$, and $Tb^{3+}$ ions. Doping concentrations ranged from 0.1–8 mol%, depending on the ion. Phosphors were synthesised via high-temperature solid-state reaction at 1000 °C for 4 hours and characterised using X-ray diffraction, photoluminescence spectroscopy, luminescence decay analysis, and quantum yield measurements.

XRD analysis showed that samples with dopant ion concentrations of up to 1 % are single-phase, but higher concentrations lead to the appearance of impurity phase peaks, which become stronger with increasing concentrations. The emission spectra revealed distinct luminescent properties for each dopant. $Bi^{3+}$-doped samples emitted a strong blue light at 420 nm, while $Dy^{3+}$-doped samples showed yellow emission at 574 nm. $Eu^{3+}$, $Pr^{3+}$, and $Sm^{3+}$-doped samples exhibited red and orange-red emissions at 611 nm, 612 nm, and 600 nm, respectively, whereas $Tb^{3+}$-doped samples emitted a prominent green light at 549 nm. In terms of optical performance, $Bi^{3+}$-doped samples achieved a maximum quantum yield of 5.80%. $Dy^{3+}$-doped samples exhibited a peak quantum yield of 3.94% and a longest decay time of 538.19 μs. $Eu^{3+}$-doped samples showed the highest quantum yield of 14.27% and a maximum decay time of 1589.42 μs. $Sm^{3+}$-doped samples reached a quantum yield of 3.61% with a decay time of 1896.76 μs. $Tb^{3+}$-doped samples demonstrated the longest decay time overall, reaching 2342 μs.

# SANTRAUKA

## VILNIAUS UNIVERSITETAS
## CHEMIJOS IR GEOMOKSLŲ FAKULTETAS

GABIJA JANUŠAUSKAITĖ

## $Bi^{3+}$, $Dy^{3+}$, $Eu^{3+}$, $Pr^{3+}$, $Sm^{3+}$ ir $Tb^{3+}$ jonais legiruoto $NaAlGeO_4$ sintezė ir liuminescencinių savybių tyrimas

Efektyvūs ir termiškai stabilūs fosforai yra svarbūs puslaidininkinių šviestukų, biovaizdinimo ir optinių jutiklių srityse. Šio tyrimo tikslas – ištirti $Na_{1-x}AlGe_{1-0,5x}O_4$ pagrindu susintetintų fosforų, legiruotų trivalenčiais $Bi^{3+}$, $Dy^{3+}$, $Eu^{3+}$, $Pr^{3+}$, $Sm^{3+}$ ir $Tb^{3+}$ jonais, liuminescencines savybes. Legiravimo koncentracijos priklausomai nuo legiruojamo jono svyravo nuo 0,1 iki 8 %. $NaAlGeO_4$ fosforų serija susintetinta aukštos temperatūros kietafazių reakcijų metodu, kaitinant junginius 1000 °C temperatūroje 4 valandas. Gauti mėginiai charakterizuoti Rentgeno spindulių difrakcijos metodu, ištirti jų sužadinimo ir emisijos spektrai, išmatuotos gesimo trukmės bei kvantiniai našumai.

XRD analizė parodė, kad mėginiai su legiruojamų jonų koncentracija iki 1 % yra vienfaziai, tačiau didesnė koncentracija sukelia priemaišinių fazių smailių atsiradimą, kurios stiprėja didėjant koncentracijai. Emisijos spektrai atskleidė skirtingas emisijos savybes kiekvienam legiruojančiam jonui: $Bi^{3+}$ jonais legiruoti mėginiai spinduliavo stiprią mėlyną šviesą ties 420 nm, o $Dy^{3+}$ – geltoną ties 574 nm. Legiravus $Eu^{3+}$, $Pr^{3+}$ ir $Sm^{3+}$ jonais, mėginiai skleidė raudoną ir oranžinę-raudoną emisiją ties 611 nm, 612 nm ir 600 nm atitinkamai. O legiruojant $Tb^{3+}$ jonais, mėginiai spinduliavo ryškią žalią emisiją ties 549 nm. Vertinant optines savybes, $NaAlGeO_4{:}Bi^{3+}$ fosforai pasiekė maksimalią 5,80 % kvantinę išeigą. $Dy^{3+}$ mėginiai pasižymėjo 3,94 % kvantine išeiga ir 538,19 µs gesimo laiku. $Eu^{3+}$ legiruoti mėginiai pasiekė aukščiausią – 14,27 % – kvantinę išeigą ir 1589,42 µs gesimo laiką. $Sm^{3+}$ legiruoti mėginiai pasižymėjo 3,61 % kvantine išeiga ir 1896,76 µs gesimo laiku. O $Tb^{3+}$ legiruoti mėginiai demonstravo ilgiausią, iš visų legiruotų jonų, gesimo laiką – net 2342 µs.